photonics

MDPI

Article

Insights on Potential Photoprotective Activity of Two Butylchalcone Derivatives: Synthesis, Spectroscopic Characterization and Molecular Modeling

Antônio S. N. Aguiar [1], Pablo G. M. Dias [1], Jaqueline E. Queiroz [2], Pollyana P. Firmino [3], Jean M. F. Custódio [4], Lucas D. Dias [1,5,*], Gilberto L. B. Aquino [2], Ademir J. Camargo [1] and Hamilton B. Napolitano [1,5,*]

1 Grupo de Química Teórica e Estrutural de Anápolis, Universidade Estadual de Goiás, Anápolis 75132-400, GO, Brazil
2 Laboratório de Pesquisa em Bioprodutos e Síntese, Universidade Estadual de Goiás, Anápolis 75132-400, GO, Brazil
3 São Carlos Institute of Physics, University of São Paulo, São Carlos 13566-590, SP, Brazil
4 Department of Chemistry and Biochemistry, University of Notre Dame, Notre Dame, IN 46556, USA
5 Laboratório de Novos Materiais, Universidade Evangélica de Goiás, Cidade Universitária, Anápolis 75083-515, GO, Brazil
* Correspondence: lucasdanillodias@gmail.com (L.D.D.); hamilton@ueg.br (H.B.N.)

Abstract: The development of photoprotective agents presents a growing interest due to skin disorders, e.g., cancer. In order to obtain natural-based compounds with potential photoprotective activity, we promote the synthesis and extensive characterization of a butylchalcone derivative (*E*)-3-(4-butylphenyl)-1-(4-methylphenyl)-prop-2-en-1-one (BMP). Moreover, we carried out a comparative analysis of two chalcones bearing a methyl (BMP) and bromo (BBP) substituent groups (at *para* position), on respective electronic structures and supramolecular arrangement, using density functional theory (DFT). Through theoretical calculations carried out by DFT, it was possible to verify its antioxidant property by the mechanisms of free radical scavenging, H-atom transfer (HAT), and one-electron transfer (ET), and their stabilities. Finally, from the analysis of chalcone's electronic transitions in the excited state calculated by the time-dependent (TD)-DFT method as well as UV-vis absorption spectra of the BMP and BBP (200–390 nm), it is possible to highlight their potential use as organic photoprotective agents.

Keywords: butylchalcone; X-ray diffraction; supramolecular arrangement; DFT; sunscreen

Citation: Aguiar, A.S.N.; Dias, P.G.M.; Queiroz, J.E.; Firmino, P.P.; Custódio, J.M.F.; Dias, L.D.; Aquino, G.L.B.; Camargo, A.J.; Napolitano, H.B. Insights on Potential Photoprotective Activity of Two Butylchalcone Derivatives: Synthesis, Spectroscopic Characterization and Molecular Modeling. *Photonics* **2023**, *10*, 228. https://doi.org/10.3390/photonics10030228

Received: 28 December 2022
Revised: 24 January 2023
Accepted: 16 February 2023
Published: 21 February 2023

1. Introduction

Due to health challenges of skin diseases, such as cancer and actinic keratoses, there is great interest in the development of photoprotective agents to avoid damaging the skin [1,2]. Moreover, these photoprotective agents should present low cost/toxicity and ultraviolet (UV) absorption property [3]. In this regard, natural product derivatives have been shown as promising photoprotective agents, e.g., plant extracts (i.e.,: *Ginkgo biloba* and *Lippia* sp.), green propolis, caffeic acids derivatives [4], and chalcones (1,3-diaryl-2-propen-1-ones) [5]. Among these natural products, chalcones represent a versatile class of natural-based compounds possessing a set of pharmacological properties, such as antioxidant [6], anticancer [7], antidiabetic [8], larvicidal [9], antibacterial [10], antiparasitic [11], anti-inflammatory [12], neuroprotective agents [13], and insecticidal [14], as well as optic properties [15–17], including photoprotective activity [18], due to their UV-absorbing and antioxidant properties.

In order to obtain chalcone-based sunscreen agents with ideal physical and chemical properties, the understanding of their molecular structure as well as structure–activity relationship plays a pivotal role. By the way, there are several examples in literature

reporting the molecular design of chalcones with different groups (electron-donating and withdrawing), such as bromine, butyl, methyl, nitro, and dimethylamino [19,20]. These modulations on molecular structures of chalcone modify their pharmacokinetic and pharmacodynamics properties as well as the properties of cosmetic agents (e.g.,: sunscreen) [5].

Herein, we described the synthesis of a butylchalcone derivative (*E*)-3-(4-butylphenyl)-1-(4-methylphenyl)-prop-2-en-1-one (BMP) and its structural description by X-ray diffraction. Moreover, we promoted a comparative analysis of two chalcones bearing methyl (BMP) and bromine (BBP) [21] substituent groups (at *para* position) on the molecular and electronic structures and on the supramolecular arrangement through density functional theory (DFT). Additionally, BMP chalcone was fully characterized by a set of spectroscopy and thermal characterizations, namely Ultraviolet–visible (UV-vis) spectroscopy, ^{1}H-^{13}C-nuclear magnetic resonance (NMR) spectroscopy, Raman spectroscopy, infrared (IR) spectroscopy, DSC analysis, and mass spectrometry (MS). The use of BMP and BBP chalcone derivatives as a potential sunscreen agent (Figure 1) was proposed on the basis of their observed optical properties.

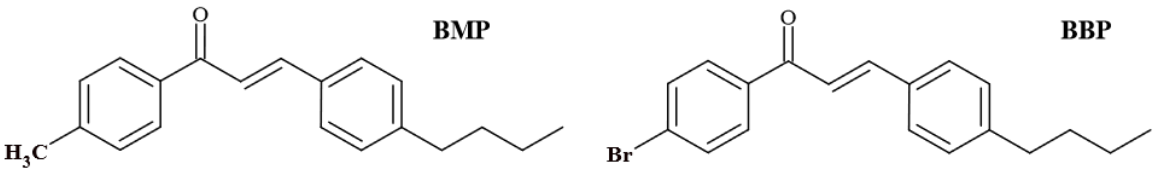

Figure 1. Molecular structures of (*E*)-3-(4-butylphenyl)-1-(4-methylphenyl)-prop-2-en-1-one (BMP) and (*E*)-3-(4-butylphenyl)-1-(4-bromophenyl)-prop-2-en-1-one (BBP).

2. Materials and Methods

2.1. Synthesis and Crystallization

All solvents and chemicals were commercially obtained from Sigma-Aldrich. Initially, 4-methylacetophenone (1 mmol; 134 mg) or 4′-bromo-acetophenone (1 mmol; 199.0 mg), 4-butylbenzaldehyde (1 mmol; 162 mg), and ethanol (1 mL) were added to a volumetric flask. Subsequently, pulverized KOH (1 mmol; 56.1 mg) was also added and the reaction was mixed by manual shaking for 3 min at 25 °C. White precipitate products were obtained, filtrated by vacuum filtration, and crystallized using ethanol. (*E*)-3-(4-butylphenyl)-1-(4-methylphenyl)prop-2-en-1-one (BMP) and (*E*)-3-(4-butylphenyl)-1-(4-bromophenyl)-prop-2-en-1-one (BBP) were obtained in 92% yield (0.92 mmol; 256 mg) and in 95% yield (0.95 mmol; 326.0 mg), respectively. Then, in a conical flask, the crystal growth of BMP and BBP were performed using dichloromethane. The BMP and BBP crystals were obtained by the slow evaporation method, keeping the mixture at 25 °C for 80 h. BMP crystals: $C_{20}H_{22}O$ (278.40 g/mol); white prism solid; and m.p.: 71.2 °C. BBP crystals: $C_{19}H_{19}BrO$ (343.26 g/mol); white prism solid; and m.p.: 109.8 °C.

2.2. Characterization

A UV-Vis spectrum was obtained using a Cary 5000 UV-Vis-NIR spectrometer and DMSO as solvent. ^{1}H and ^{13}C NMR spectra were obtained on a Bruker Avance 500 MHZ NMR spectrometer using TMS and $CDCl_3$ as the internal standard and solvent, respectively. Raman analysis was performed using a WITec Alpha 300 RAS microscope (WITec, Ulm, Germany), excitation wavelength at 785 nm, and a detection range of 100–4000 cm^{-1}. The spectra were collected with a 20× magnification objective (Zeiss, Jena, Germany). Spectra were recorded with the integration time of 30 s and 2 accumulations. Obtained spectra were processed and analyzed using WITec Project FOUR and Origin 2016 software. DSC analysis was performed in a 214 Polyma, Netzsch equipment equipped with platinum crucibles. BMP sample (5.08 mg) was added in the crucibles and the following program was applied: temperature range: 20–200 °C; heating rate of 10 °C·min^{-1}, under a N_2 atmosphere with a flow of 40 mL·min^{-1}. GC-MS spectrum was obtained in a Shimadzu (QP2010 Ultra)

spectrometer, EI mode, and equipped with a CBP-5 (30 × 0.25 × 0.25) column. Moreover, the following parameters were used: injection volume: 1.0 µL (split mode) and helium as drag gas (1.0 mL.min^{-1}); injector temperature: 280 °C; detector temperature: 310 °C; initial oven temperature: 100 °C (for 2 min) followed by a heating ramp of 30 °C.min^{-1} until 300 °C. The IR analysis was carried out using a Perkin Elmer (8400S FT-IR) spectrometer using the wavenumber range of 400–4000 cm^{-1} and KBr technique.

2.3. X-ray Diffraction Analysis

A suitable crystal of BMP was selected, kept at 273 K, and the X-ray diffraction was collected on a Bruker APEX-II CCD diffractometer with wavelength radiation MoKα λ = 0.71073 Å. The crystal size used was 0.21 × 0.23 × 0.04 mm^3. The structure was solved by direct methods with the intrinsic phasing method (SHELXT) [22] using Olex2 1.3 version [23] and refined by least-squares minimization with SHELXL [24]. All hydrogen atoms were fixed at the calculated position, and potential hydrogen bond interactions were verified through Platon [25] and Crystal Explorer software [26]. The BMP and BBP structures data were deposited in the Cambridge Crystallography Data Centre (CCDC) under codes 2232935 and 2069836, respectively.

2.4. Molecular Modeling

Theoretical calculations were carried out by DFT [27,28], implemented in the G16 [29] software package, using the hybrid exchange and correlation functional with long range correction, M06-2X [30], combined with the basis set 6-311++G(d,p), in gas phase. The obtained geometric parameters were compared to the experimental ones. The chalcones have substituent groups –CH_3 (electron-donating) and –Br (electron-withdrawing) at the *para* position of the aromatic B ring. Moreover, the molecular structures were compared to verify the effects of these groups on their molecular conformations. Frontier molecular orbitals (FMO) [31], highest occupied molecular orbital (HOMO), and lowest unoccupied molecular orbital (LUMO) were obtained. The kinetic stabilities and chemical reactivity of the butylchalcone derivatives were compared. Molecular electrostatic potential maps contributed to the global electrophilicity analysis through their electronic isodensity surfaces. The electrostatic potential $V(\mathbf{r})$ [32] at point $\mathbf{r}$ is defined as

$$V(\mathbf{r}) = \sum_{\alpha} \frac{Z_\alpha}{|\mathbf{r}_\alpha - \mathbf{r}|} - \int \frac{\rho(\mathbf{r}')}{|\mathbf{r}' - \mathbf{r}|} d\mathbf{r}', \quad (1)$$

where Z_α is the charge of nuclei α at point $\mathbf{r}_\alpha$ and $\rho(\mathbf{r}')$ is the charge density at point $\mathbf{r}'$. Furthermore, from the MEP map it is possible to predict the possible regions where intermolecular interactions occur.

The local electrophilicity of both molecules was determined by the Fukui function [33,34] and then it was possible to predict the molecular regions in which chalcones act as antioxidant agents. Based on Fukui indices, the possible radicals formed in the free radical scavenging processes were analyzed through spin density calculations [35,36]. This was started from the BMP- and BBP- optimized structures to optimize the respective radicals using the same level of theory used previously. The radical structures deformation energies were included in the results we obtained for the analysis of the chalcones antioxidant potential [37]. NBO [38] analysis was carried out to determine the radicals stability by the hyperconjugation energy [39], estimated by the second-order perturbation formula,

$$E^{(2)}_{i \to j^*} = -n_\sigma \frac{\left\langle \sigma_i \middle| \hat{F} \middle| \sigma_j^* \right\rangle^2}{\varepsilon_{j^*} - \varepsilon_i} = -n_\sigma \frac{F_{ij}^2}{\varepsilon_{j^*} - \varepsilon_i}, \quad (2)$$

where $\langle \sigma | F | \sigma^2 \rangle$ or F_{ij}^2 is the Fock matrix element between the natural bond orbitals i, and j; ε_{σ^*} is the energy of the antibonding orbital σ^*, and ε_σ is the energy of the bonding orbital σ; n_σ stands for the population occupation of the σ donor orbital.

2.5. Supramolecular Arrangement

The butylchalcone derivatives (BMP and BBP) supramolecular arrangements were determined by the Hirshfeld surfaces (HS) [40] and 2D fingerprint plots [41], providing information about the intermolecular interaction patterns by color mapping, in addition to describing the specific properties of the surfaces. The HS indicates the partition of the crystal electron density and the molecular fragments of the space occupied. The 2D fingerprint plots indicate the percentages of the strength of interactions involved in the crystal packing modes [42]. The donor and recipient regions are based on the normalized function of the distance to the nearest inner surface nucleus. The distance from the point to the nearest nucleus outside the surface represents the regions of space where molecules are in contact with each other. Furthermore, quantum theory of atoms in molecules [43] (QTAIM) calculations showed the character of these interactions, through the analysis of the topological parameters. For these theoretical calculations, the inputs were constructed from the crystallographic data at the M06-2X/6-311++G(d,p) level of theory, in which the atomic coordinates were kept fixed. The NBO analysis was carried out to determine the interactions stability by the hyperconjugation energy, (Equation (2)).

2.6. Analysis of Photoprotective Property

To understand the BMP and BBP electronic transitions, calculations of the electronic absorption spectra were carried out using implicit solvation (DMSO) by polarizable continuum model (PCM) as implemented in G16 [29]. From the optimized structure, the TD-DFT method was used, with the functional CAM-B3LYP with the basis set 6-311++G(d,p), and the data obtained for the electronic transitions were compared to the data experiments of both chalcones. UV-Vis spectra of the chalcones (BMP and BBP) were obtained using a Cary 5000 UV-Vis-NIR spectrometer and DMSO as solvent. The analysis of the range of UV-vis absorption was performed using Origin 2016 software.

3. Results

3.1. Synthesis and Characterization

The BMP chalcone was obtained in 92% yield according to Section 2.1 via the Claisen–Schmidt condensation approach (Scheme 1).

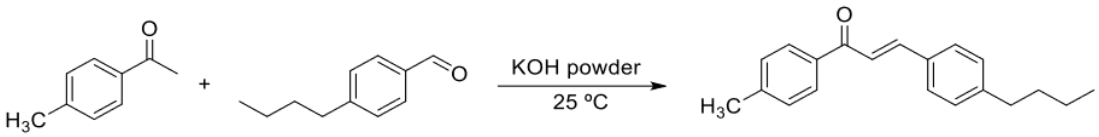

Scheme 1. General procedure for BMP synthesis.

Figure S1 shows UV spectrum of BMP with an absorption band between 293 and 385 nm and a maximum absorption at 308 nm. Raman spectroscopy also was used to characterize and determine the quality of the BMP crystals (Figure S2). Spectra for each crystal type were normalized to a certain peak (the exact position of the peak is indicated by arrows on the graphs and in the figure legends). For the Raman spectrum of BMP, the C–H stretching vibrations were observed at 1300–1000 cm^{-1}, showing a strong Raman intensity. The C-H out-of-plane deformations were observed at 740, 759, 800, 836, 896, 965, and 984 cm^{-1} for the BMP crystal (Figure S2). Moreover, peaks at 1256, 1303, 1333, 1376, 1425, and 1432 cm^{-1} for BMP crystal were observed and assigned to C–C stretching vibrations. A sharp band at 1604 cm^{-1} was also observed and assigned to ethylenic bridge vibrations for BMP. The C=O vibrations also were observed as a weak Raman band at 1666 for BMP. The C=O stretching vibration is further influenced by intermolecular hydrogen bonding between the C=O group and phenyl ring, which may explain the weak Raman band observed for the BMP chalcone.

Moreover, aiming to characterize the molecular structure of the BMP and its purity, ^{1}H-NMR (Figure S3) and ^{13}C-NMR (Figure S4) were carried out. The chemical shifts are

shown below: ^{1}H NMR (500 MHz, $CDCl_3$) δ 7.97 (d, *J* = 8.2 Hz, 2H), 7.8 (d, *J* = 15.7 Hz, 1H), 7.59 (d, *J* = 8.2 Hz, 2H), 7.54 (d, *J* = 15.7 Hz, 1H), 7.33 (d, *J* = 8.0 Hz, 2H), 7.26 (d, *J* = 8.1 Hz, 2H), 2.68 (d, *J* = 7.8 Hz, 2H), 2.46 (s, 3H), 1.64 (dq, *J* = 12.9, 7.6 Hz, 2H), 1.45–1.35 (m, 2H), 0.97 (t, *J* = 7.4 Hz, 3H); ^{13}C NMR (126 MHz, $CDCl_3$) δ 190.15, 146.01, 144.59, 143.54, 135.78, 132.46, 129.34, 129.31, 129.08, 128.66, 128.50, 121.07, 35.65, 33.44, 22.38, 21.72, 13.99.

Figure S5 presents the DSC thermogram of the BMP crystals which show a sharp exothermic peak (at 71.2 °C). This peak indicates direct melting of the BMP crystal phase to the isotropic liquid phase. Furthermore, Figure S6 shows the MS spectrum of BMP chalcone presenting the following data: GC-MS (EI): r.t./min (m/z) = 9.3 min (277, 263, 235, 221, 192, 165, 131, 119, 91, 65, and 41). BMP chalcone also was characterized by IR spectroscopy (Figure S7). From the analysis of the IR spectrum, the following typical bands are presented: 2967 υ(Csp2-H); 2923 υ(C-H); 1657 υ(C=O); 1595 υ(C=C); 1422 υ(C=C) aromatic ring; 987 υ(CH=CH). In addition, the BBP chalcone was also fully characterized by ^{1}H- and ^{13}C-NMR spectroscopy, Raman spectroscopy, IR spectroscopy, DSC analysis, and MS and the data are described in our publication [21].

3.2. Solid State Description

The BMP molecule has a $–CH_3$ group linked in the *para* position of the A ring and an n-butyl group, also in the para position attached to the B ring of the chalcone. The structural information and interactions of the BMP and the ORTEP graph were generated using the Olex2 [23] software (Figure 2), so that the atomic ellipsoids are similar in size, indicating the absence of disorder [44]. The BMP molecule was crystallized in the orthorhombic crystalline system. Unusual bond lengths and angles and torsions were based on conformation observed by the statistical analyzer Mogul software. The main crystallographic refinement data are presented in Table 1.

Table 1. Crystallographic data and structure refinement for BMP and BBP.

Crystal Data	BMP	BBP
Chemical formula	$C_{20}H_{22}O$	$C_{19}H_{19}OBr$
Molecular weight (g/mol)	278.37	343.25
Crystal system	orthorhombic	orthorhombic
Space group	*P*bca	*P*bca
a (Å)	11.341(3)	11.3065(12)
b (Å)	8.1445(19)	8.1831(9)
c (Å)	33.628(8)	33.892(4)
α (°)	90	90
β (°)	90	90
γ (°)	90	90
Volume (Å^3)	3106.2(12)	3135.8(6)
Z	8	8
Radiation type	Mo *Kα* (λ = 0.71073)	Mo *Kα* (λ = 0.71073)
$R[F^2 > 2\sigma(F^2)]$; $wR(F^2)$	R_1 = 0.0545, wR_2 = 0.1346	R_1 = 0.0317, wR_2 = 0.0620
S	1.025	1.035
Dimentions (mm)	0.23 × 0.21 × 0.04	0.226 × 0.197 × 0.044

Chemically, molecular planarity in chalcones is a parameter that is related to donor–acceptor interactions through its main chain and through π conjugation along the charge transfer [45]. This parameter is closely related to molecular properties, such as electron transfer, non-linearity, solubility, molecular packing, and melting point. However, we observed that the BMP molecule has a non-planar structure (Figure S8a), so that the angle formed between the aromatic rings is 47.38°. In the case of the BBP molecule [21], which is also non-planar (Figure S8b), the observed angle between the aromatic rings is 0.7% smaller compared to BMP. The non-planarity of the molecules decreases the crystal packing energy and the melting point, in addition to contributing to a better aqueous solubility of the chalcones.

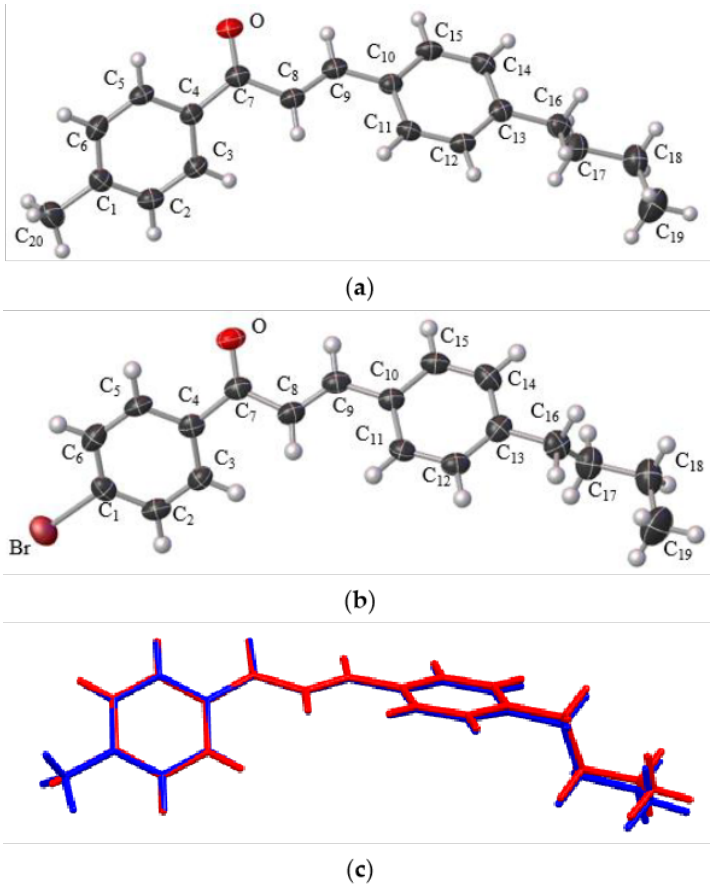

Figure 2. Ortep diagram showing (**a**) BMP and (**b**) BBP chalcones in the asymmetric unit drawing with 75% probability ellipsoid. (**c**) Overlap of BMP (in blue) e BBP (in red) chalcones molecular structures (RMS = 0.0198 Å).

The conformational between chalcone structures showed that the substituent group does not change significantly their molecular geometry. For bond lengths (see the graph in Figure 3a), compression of the C_8=C_9 bond of the BMP bridge by 3.82% was observed, by the substitution of the Br atom by the –CH_3 group. Furthermore, as expected, the volume of the Br atom directly impacts the C_1–Br length by approximately 20.86%. In the case of bond angles (Figure 3b), it was observed that C_1–C_2–C_3 and C_5–C_6–C_1 of the benzene ring A increased by 1.98 and 1.89%, respectively, while C_6–C_1–C_2 decreased by 3.08%. The torsional angles also did not change significantly along the carbon chains of the chalcones. A small decrease of 2.13 and 1.14% was observed in C_5–C_4–C_7–O_1 and C_{15}–C_{10}–C_9=C_8, respectively. In the case of bond angles, it was observed that C_1–C_2–C_3 and C_5–C_6–C_1 of the benzene ring A increased by 1.98 and 1.89%, respectively, while C_6–C_1–C_2 decreased by 3.08%. The torsional angles also did not change significantly along the carbon chains of the chalcones. A small decrease of 2.13 and 1.14% was observed in C_5–C_4–C_7–O_1 and C_{15}–C_{10}–C_9–C_8, respectively. The chalcone bridge is 28° out of the plane of ring A and 19° out of the plane of ring B, and both rings form planes of 47° to each other. Through the overlap of BMP and BBP molecules, shown in Figure 2c, it is possible to observe that the torsional angles vary little in both structures.

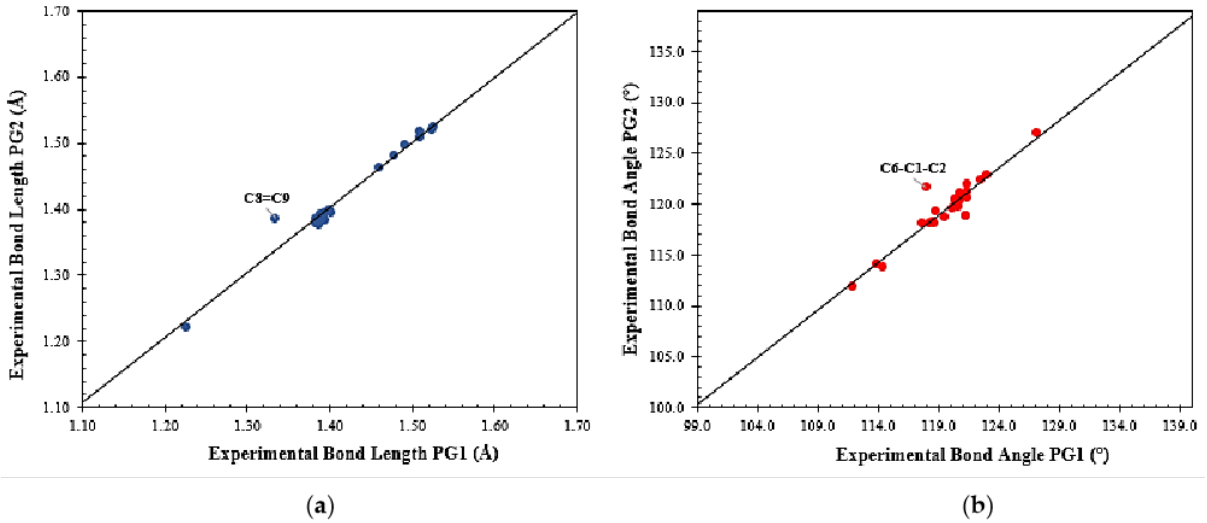

Figure 3. Scatter plots comparing experimental values of bond lengths (**a**) and bond angles (**b**) in BMP and BBP chalcones.

The theoretical geometric parameters of the results were compared to the experimental data, through the mean absolute percentage deviation,

$$\text{MADP} = \frac{100}{n}\sum_{i=1}^{n}\left|\frac{\chi_{DFT}-\chi_{XRD}}{\chi_{XRD}}\right|, \quad (3)$$

where χ_{DFT} and χ_{XRD} represent the theoretical and experimental geometric parameters, respectively. The results showed that the level of theory used is adequate to describe the chalcones BMP and BBP. The MADP values for bond lengths were, respectively, 0.388% in BMP, with Pearson's correlation coefficient equal to R^2 = 0.9981, and 0.499%, with R^2 = 0.9954, in BBP. Figure 4a,c show the scattering of the bond lengths in chalcones, comparing theoretical and experimental values. The graphs show that the deviations were very small, highlighting the C_8=C_9 bond in BBP, which is approximately 3.4% smaller for the molecule maintained in a vacuum. In the case of bond angles, the MADP values were 0.565% (R^2 = 0.9233) in BMP and 0.516% (R^2 = 0.9329) in BBP. Figure 4b,d show the scattering of the theoretical *versus* experimental bond angles. The largest deviations occurred with average increases of 1.8% and 3.7% in C_{14}–C_{13}–C_{16} and C_{13}–C_{16}–C_{17}, respectively, and with the average decreases of 1.6%, 1.6%, and 1.4% in C_{12}–C_{13}–C_{16}, C_{16}–C_{17}–C_{18}, and C_{17}–C_{18}–C_{19}. Figure 4b,d show the theoretical angles behavior compared to experimental ones.

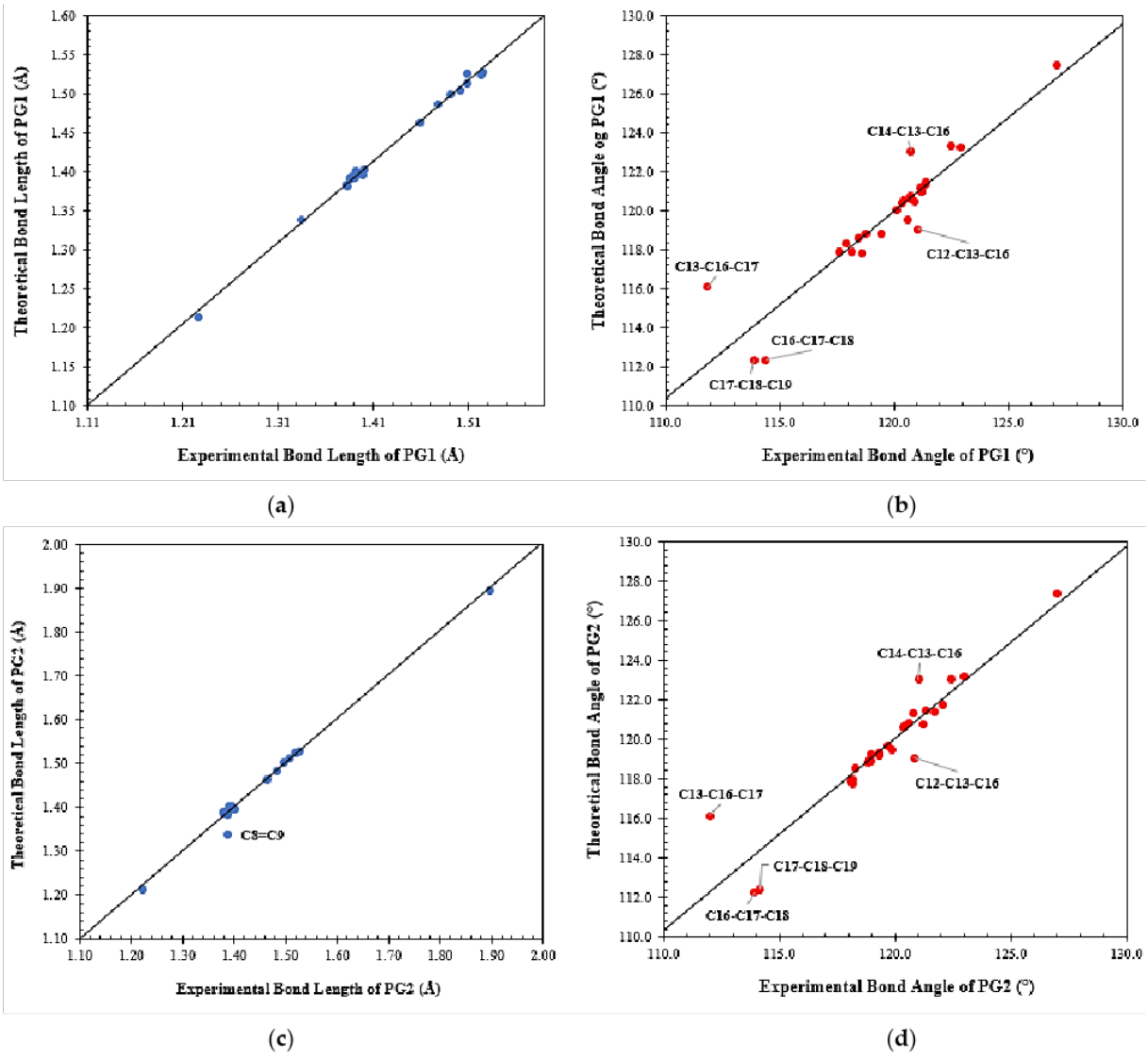

Figure 4. Scatter plots comparing experimental and theoretical values of bond lengths (**a**,**c**), and bond angles (**b**,**d**) in BMP and BBP chalcones.

3.3. Molecular Modeling Analysis

From the calculations of electron density $\rho(\mathbf{r})$, it was possible to determine some electronic properties of the molecules of the chalcones BMP and BBP. The delocalized FMO isosurfaces are shown in Figure 5 and the HOMO and LUMO energies are shown in Table 2. The data showed that the HOMO energy in BMP is ≈2.0% lower than the HOMO energy in BBP. A slight difference infers a slightly more basic character to the brominated chalcone. On the other hand, the energy of the LUMO of BMP is ≈14.8% lower than that of the LUMO of BBP, conferring a character that is consequently more acidic to the former. The energy gaps ($\Delta E_{HOMO\text{-}LUMO}$) of the HOMO and LUMO orbitals also indicated that the $-CH_3$ substituent group makes the BMP molecule slightly more stable than BBP (Table 2).

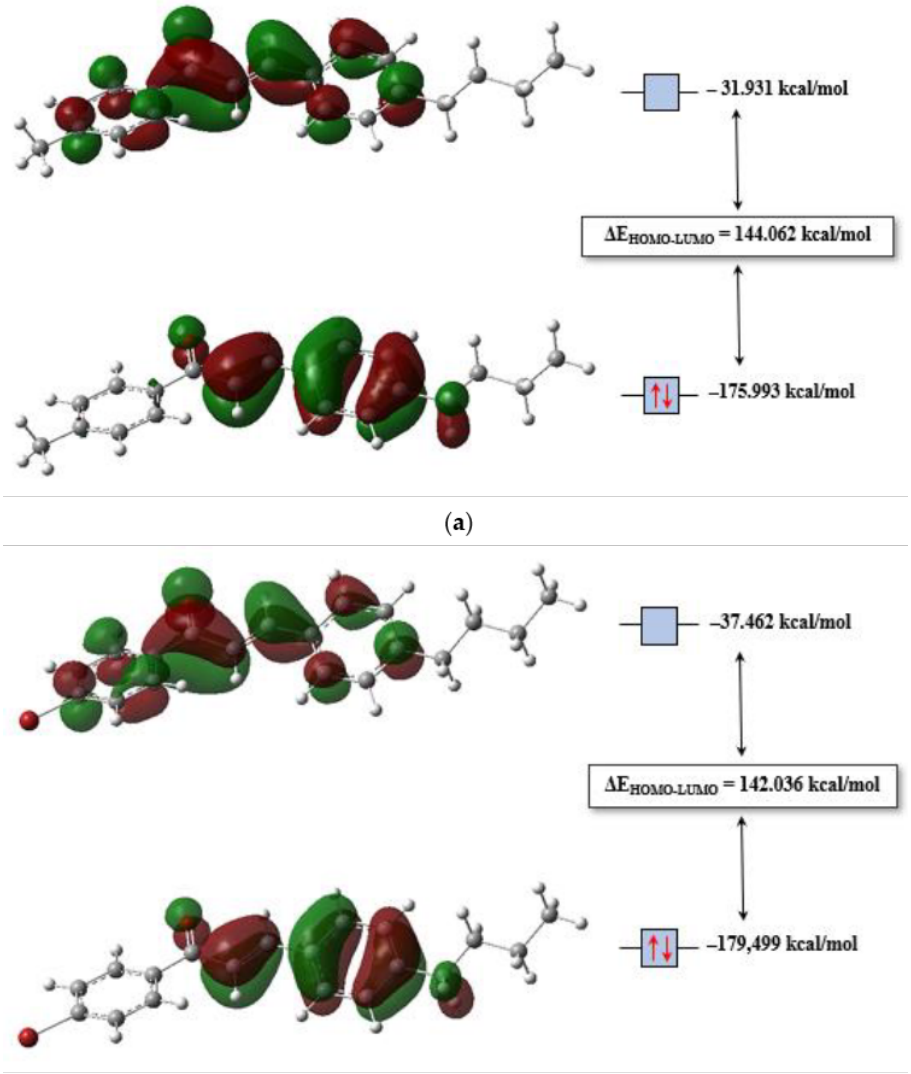

Figure 5. HOMO and LUMO plots for (**a**) BMP and (**b**) BBP obtained at M06-2X/6-311++G(d,p) level of theory.

Table 2. Reactivity indices for BMP and BBP chalcones, obtained at M06-2X/6-311++G(d,p) level of theory.

DESCRIPTORS	CNP-OM (kcal/mol)	CNP-CL (kcal/mol)
E_{HOMO}	−175.993	−179.499
E_{LUMO}	−31.931	−37.462
$\Delta E_{HOMO-LUMO}$ *	144.062	142.036
Ionization Energy (I)	175.993	179.499
Electronic Afinity (A)	31.931	37.462
Electronegativity (χ)	103.962	108.480
Chemical potential (μ)	−103.962	−108.480
Chemical hardness (η)	144.062	142.036
Electrophilicity index (ω)	37.512	41.426

* The energy gap is the difference between the HOMO and LUMO energies, $\Delta E_{HOMO-LUMO} = E_{LUMO} - E_{HOMO}$.

Based on the FMO energies values, the chemical hardness,

$$\eta = \frac{1}{2}\left(\frac{\partial^2 E}{\partial N^2}\right)_v = \frac{I-A}{2}, \quad (4)$$

of the chalcones was determined, which showed that the orbitals in BMP are 1.4% harder. This difference indicates that the orbitals of this molecule are less polarizable than the orbitals of BBP. In addition, the calculated values for the chemical potential,

$$\mu = \left(\frac{\partial E}{\partial N}\right)_v = -\frac{I+A}{2} = -\chi, \quad (5)$$

showed that BMP has a greater ability to transfer charge during chemical processes since it has a 4.2% higher μ value, which also justifies its slightly more basic character. In Equations (4) and (5), E is the energy of the system, N is the number of electrons, v is the external potential, $I = -E_{HOMO}$ is the ionization potential, and $A = -E_{LUMO}$ is the electron affinity.

To measure the electrophilic nature of molecules, global electrophilicity indices were also calculated by the expression,

$$\omega = \frac{\mu^2}{2\eta}. \quad (6)$$

A quantitative characterization was carried out for several organic molecules, in which the theoretical results showed that, for strong electrophiles $\omega > 1.5$ eV (or $\omega > 35$ kcal/mol), for moderate electrophiles 0.8 eV $< \omega <$ 1.5 eV (or 18 kcal/mol $< \omega <$ 35 kcal/mol) and, finally, for marginal electrophiles $\omega < 0.8$ eV (or $\omega <$ 18 kcal/mol) [46,47]. The BMP and BBP compounds are strong electrophiles, so the latter is about 9.4% more electrophilic. These results make sense since the substituent –Br atom is a more electronegative atom than the carbon of the $–CH_3$ group, resulting in a molecule with higher electronegativity, χ. To determine the localized electrophilicity in both compounds, the Fukui function was used to determine the sites of nucleophilic,

$$f^+ = \left[\frac{\partial \rho(r)}{\partial N}\right]^+_v, \quad (7)$$

electrophilic,

$$f^- = \left[\frac{\partial \rho(r)}{\partial N}\right]^-_v, \quad (8)$$

and radical

$$f^0 = \left[\frac{\partial \rho(r)}{\partial N}\right]^0_v. \quad (9)$$

attacks. The most commonly used theory for the determination of Fukui indices is the finite difference approach, proposed by Parr and Yang [48], which determines that the Fukui indices are obtained from the calculations of the independent molecular orbitals for the neutral species and two ionic species, maintained under fixed external potential.

The isosurfaces obtained from the f^+, f^-, and f^0 functions are shown in Figure 6. Through these results, it is possible to observe that, in both chalcones, the charge density is high in the carbonyl O and C_7 atoms, in the C_1 atom of ring A, and the C_{13} atom of ring B, making these regions susceptible to nucleophilic attack (Figure 6a,d). In the case of C_1, the $–CH_3$ and –Br substituent groups throw electrons to the benzene ring by inductive and mesomeric effects, respectively. By MEP map (Figure 7a), it was possible to verify that the charge density is reduced on the $–CH_3$ group in BMP (blue color), due to the electron donor effect; in the Br region, in BBP, we observed that the charge density is reduced on the side opposite the C–Br bond, but slightly increased on the bond (Figure 7b), since the –Br substituent group attract electrons from the ring by induction and throws by resonance. In

the carbonyl of the aliphatic portion, the high charge density is due to the resonance effect produced by the π electrons present in this region. The MEP maps showed that the charge density is high in the O atom region (red surface color), resulting in a nucleophilic region of the molecules, both in BMP and BBP. In ring B, the *n*-butyl substituent group also throws electrons to the benzene ring by an inductive effect, increasing the charge density on the C_{13} atom.

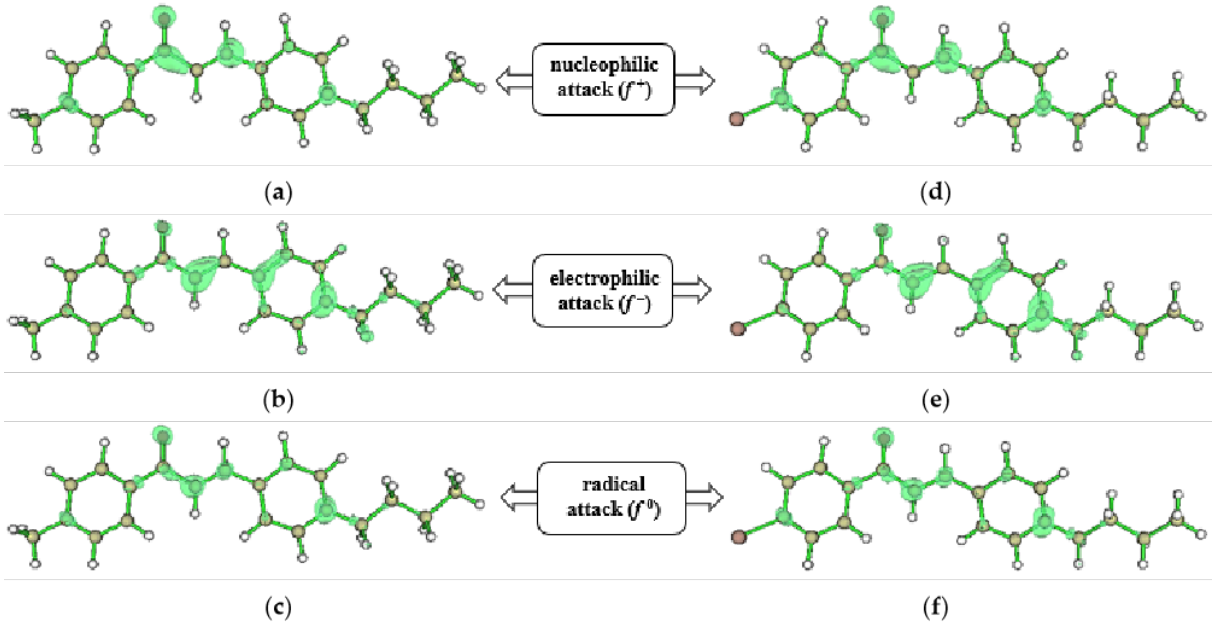

Figure 6. Isosurfaces of the (**a**,**d**) f^+, (**b**,**e**) f^−, and (**c**,**f**) f^0 functions indicating the nucleophilic, electrophilic, and radical attack regions, respectively, for BMP and BBP molecules, calculated at value of 0.5.

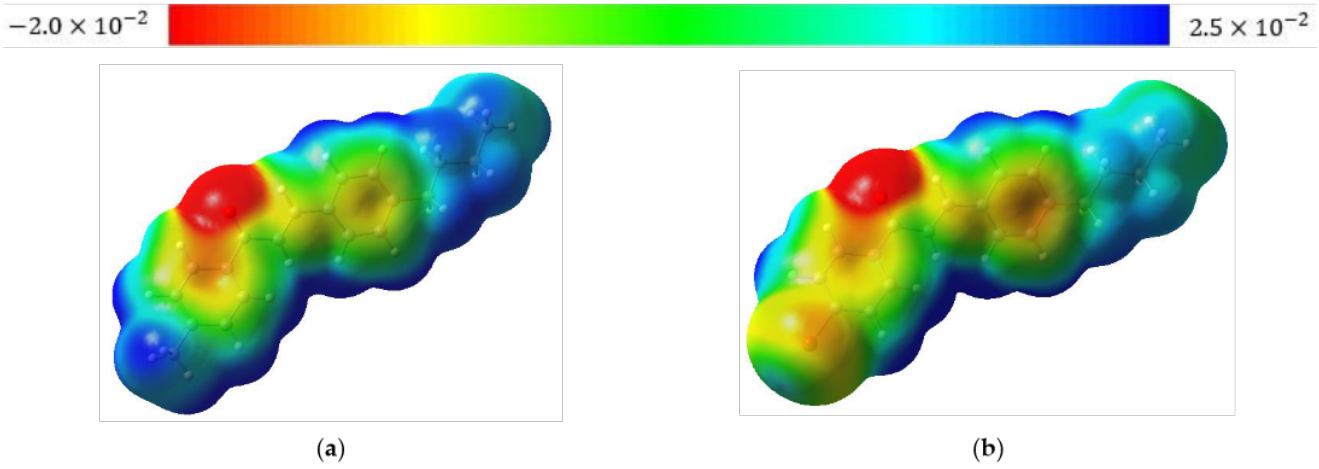

Figure 7. MEP surface at ρ(r) = 4.0×10^{-4} electrons/Bohr^3 contour of the total SCF electronic density for (**a**) BMP and (**b**) BBP at the M06-2X/6-311++G(d,p) level of theory.

According to the isosurfaces generated by the f^- function, electrophilic attacks can occur on the C_8 atoms of the aliphatic portion of the chalcones and on the C_{10} and C_{13} atoms of the B ring (Figure 6b,e). The π electrons present in the C_8–C_9 bond of the aliphatic portion of the chalcones resonate with the π electrons of the respective B rings, forming a conjugated π system. This electronic effect, together with the mesomeric effect produced by

the O atom of the carbonyl group, minimizes the charge density on the C_8 atom, making it an electrophilic region of the BMP and BBP molecules. The Mulliken atomic charges show that the C_8 atom is positive, which means that the charge density on it is low. The same occurs on the C_{10} and C_{13} atoms of the benzene ring, whose atomic charges are positive. These data confirm the electrophilic character of the molecules in these regions.

Finally, the isosurfaces produced by the f^0 function showed that O, C_8, C_9, and C_{13} atoms are susceptible to radical attacks on BMP and BBP molecules. Researchers have reported that chalcones, as well as their analogues, have antioxidant activity [49], due to the keto-vinylene group –(CO)–CH=CH– in the aliphatic region [50], in addition to hydroxyl and phenyl substituents on the benzene ring. Thus, the Fukui indices for radical attacks corroborate the data in the literature.

There are two main mechanisms that describe the antioxidant activity of compounds [51]. The first mechanism is related to the H-atom transfer (HAT) from the antioxidant molecule (A−H) to a free radical (R·), such that the antioxidant becomes a radical,

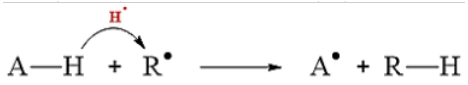

Thus, based on the results for the f^0 function, we observed the formation of two radicals that are possibly formed in the free radical scavenging activity of our chalcones, by the HAT mechanism (Scheme 2). The first (radical 1) arises from homolytic scission of the C_α–H bond (C_α = C_8), while the second (radical 2) arises from homolytic scission of the C_β–H bond (C_β = C_9). These radicals are shown in Scheme 2. The spin densities isosurfaces showed that the respective unpaired electrons are delocalized in the radicals 1 of both chalcones (Figure 8a,d). Thus, they can migrate from the C_α atom to the carbonyl O atom by resonance, so that the ground state of these radicals can then be represented as a superposition of two structures

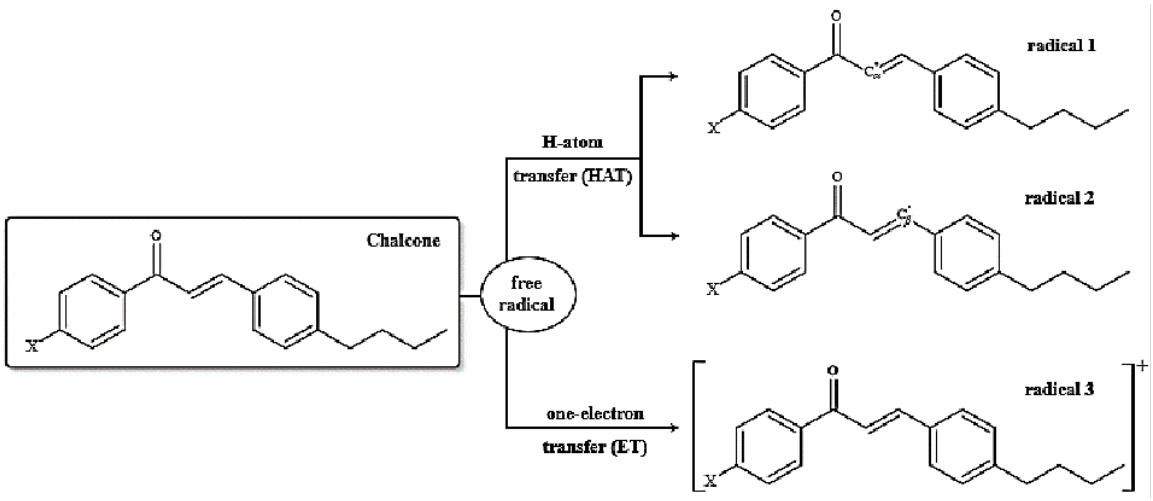

Scheme 2. Antioxidant activity mechanisms of BMP and BBP chalcones. Chalcone molecule is attacked by the free radical and can follow path I, where it transfers an H-atom to R·, or path II, where it transfers one electron to R·.

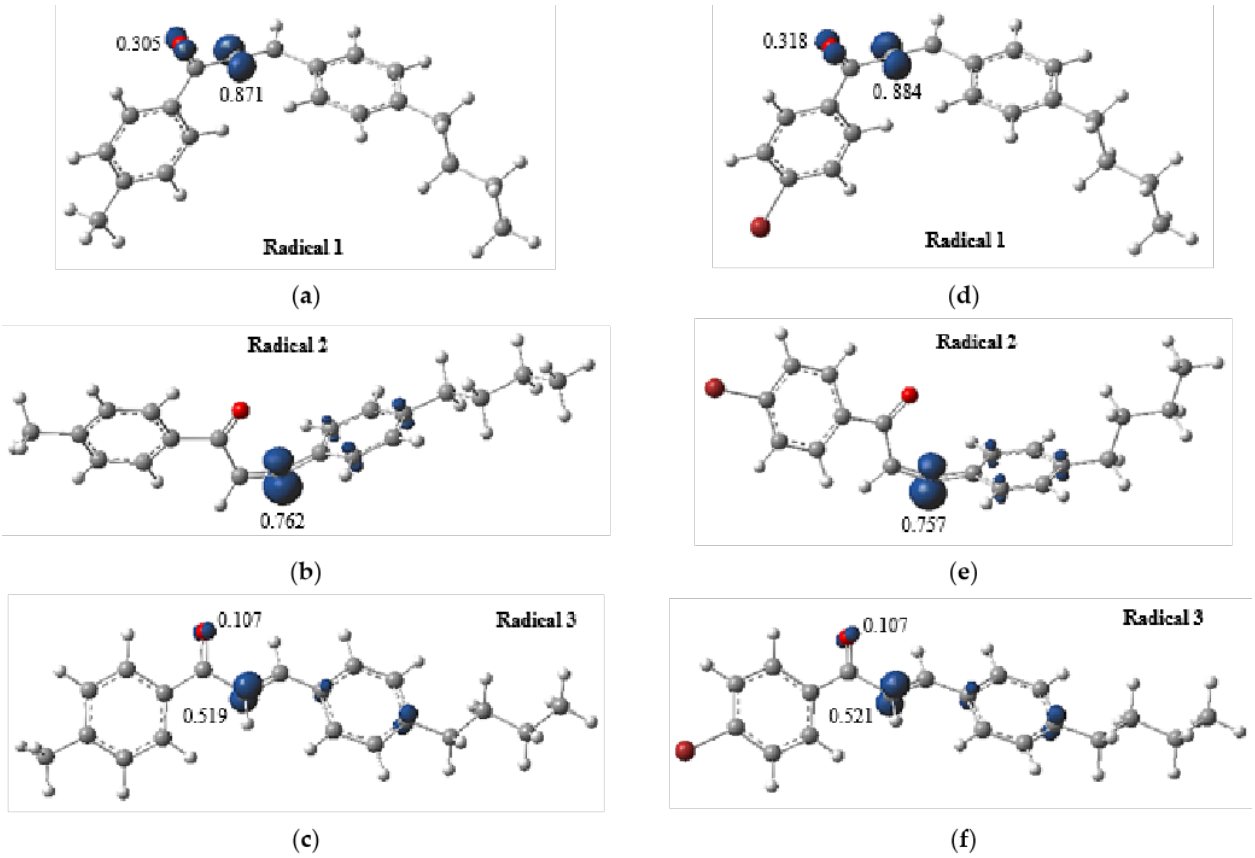

Figure 8. Electron spin densities isosurface at ρ(r) = 4.0 × 10^{-2} electrons/Bohr3 contour of the total SCF electronic density for (**a**,**b**,**c**) BMP and (**d**,**e**,**f**) BBP radicals at the M06-2X/6-311++G(d,p) level of theory.

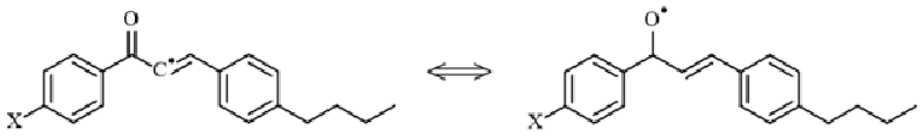

whose wave functions are represented by the linear combination

$$\Psi = c_1\psi_{C_\alpha} + c_2\psi_O. \quad (10)$$

However, the spin density calculations showed that the unpaired electron probability being located on the C_α atom is, on average, 2.8 times greater than on the O atom. In both chalcones, the unpaired electron on the C_α and O atoms are housed in a *p* orbital, whose occupancies are, respectively, 0.74*e* and 0.95*e*. NBO analysis showed that the stabilizing energies $E^{(2)}$ obtained for radicals 1 are very low, indicating that radicals are electronically unstable. The hyperconjugation that most contributes to radical stability is $\pi(C_{10}–C_{15}) \rightarrow \pi^*(C_8–C_9)$. However, the $E^{(2)}$ values obtained for the stability of radicals 1, with the unpaired electron housed to the C_α atom, were 7.06 kcal/mol in BMP and 7.45 kcal/mol in BBP. For the unpaired electron housed to the O atom, the hyperconjugation that most contributes to the stability of radicals 1 is $\pi(C_7–C_8) \rightarrow \pi^*(C_7–O)$, whose stabilizing energies were 3.62 kcal/mol in BMP and 3.61 kcal/mol in BBP. $E^{(2)}$ values justify the greater unpaired electron probability being on the C_α atom. Furthermore, data from the NBO analyses in Table S1 (supplementary material) showed that BBP is slightly more stable than BMP.

In the case of radicals 2, the spin density calculations showed that the unpaired electrons are allocated preferentially over the C_β atom, where $\rho(C_\beta) \approx 0.76$. However, these electrons are also delocalized, being able to resonate with the B ring of chalcones (Figure 8b,e), forming a conjugated π system, and being able to be allocated in atoms C_{11}, C_{13}, and C_{15}. The unpaired electron on the C_β atom is housed in the hybrid orbitals $sp^{10.31}$ in BMP and $sp^{10.72}$ in BBP, where the occupancies are 0.82*e*. The low $E^{(2)}$ values obtained indicate that the radicals 2 of both chalcones are also electronically unstable. The hyperconjugation that most contributes to the stability of these radicals is $\sigma(C_8–H) \rightarrow \sigma^*(C_9–C_{10})$, where the stabilizing energies obtained are 2.35 kcal/mol in BMP and 4.02 kcal/mol in BBP. From $E^{(2)}$ values, shown in Table S1, we can conclude that radical 2 in BBP is slightly more stable.

In the HAT mechanism, the reactivity of an antioxidant compound can be estimated by calculating the C–H bond dissociation enthalpy,

$$\Delta H^0(C-H) \;=\; H^0(A-H) - \left[H^0(A\cdot) + H^0(H\cdot)\right]. \tag{11}$$

where C is the C_α and C_β atoms. The lower the ΔH^0 value, the higher the expected antioxidant activity for the compound. In the case of BMP and BBP, the ΔH^0 values obtained for the C_α–H bond homolytic cleavage for the formation of radical 1 were 98.8 and 97.4 kcal/mol, respectively, and for the C_β–H bond homolytic cleavage for the formation of radical 2 were 97.7 and 96.5 kcal/mol. It was verified that by the $\Delta H^0(O-H)$ values, for a group of phenols, that the O–H bonds homolytic cleavage varied between 78.2 and 88.3 kcal/mol, and for a group of phenolic chalcones the values of ΔH^0(O–H), for the cleavage of the same bond, varied between 72.9 and 84.6 kcal/mol [52]. Therefore, despite having presented ΔH^0 values slightly higher than those observed in the literature, we noticed that chalcones BMP and BBP have antioxidant potential. Furthermore, homolytic cleavage of O–H bonds is not the only way for chalcones to exhibit free radical scavenging activity.

The second mechanism describes the one-electron transfer (ET) from the antioxidant (A) to the free radical (R·), such that A becomes a cation radical ($A\cdot^+$)

The spin density calculations showed that, by the ET mechanism, the unpaired electrons in the chalcones radicals 3 (Scheme 2) are preferentially allocated over the respective C_α atoms, where $\rho(Ca) \approx 0.52$. However, the isosurfaces showed that they can also be found located on atoms of O, where $\rho(O) \approx 0.11$, and of C_{13}, where $\rho(C_{13}) \approx 0.27$. These data corroborate the regions of radical attacks obtained by the f^0 function. For the ET mechanism, the evaluation of the antioxidant activity of the compound must be carried out through the ionization potential (IP), by the expression

$$\mathrm{IP} \;=\; E_0\left(A\cdot^+\right) - E_0(A-H), \tag{12}$$

where $E_0(A-H)$ is the total energy of the antioxidant and $E_0(A\cdot^+)$ is the total energy of the corresponding radical cation. The lower the IP values, the greater the antioxidant activities of a molecule. The values calculated for the IP of the chalcones were 185,351 kcal/mol (BMP) and 188,732 kcal/mol (BBP). Phenolic chalcones showed a mean IP value of 174 kcal/mol [53], the IP experimental value for phenol is 196 kcal/mol, and for glutathione, the IP value is 212 kcal/mol [53]. Thus, we can infer that the chalcones evaluated in this work are potential antioxidant agents.

The BMP supramolecular arrangement on *bc* plane has a *zig-zag* form with no classic hydrogen bonds. Similarly, the molecules in BBP also assume this structural configuration, performing no classic hydrogen bonds. It was observed that both arrangements carry out $C_3–H\cdots O_1$, $C_8–H\cdots O_1$, $C_{15}–H\cdots C_{13}$, and $C_{17}–H\cdots H–C_{18}$ interactions. By BMP HS, it

was possible to verify that in the first two interactions (Figure 9a), the contacts between the H and O atoms correspond to the sum of the van der Waals radii and occur at 2753 and 2767 Å, respectively. Such contacts are also present in the supramolecular arrangement of BBP (Figure 9b). However, in the first interaction (C_3–H$\cdots$$O_1$), the contacts occur at a distance smaller than the sum of the van der Waals radii, being 3.3% smaller than the same interaction in BMP. The C_8–H$\cdots$$O_1$ interaction is also lower in BBP (≈1.6%). In both compounds, the Hirshfeld surface showed that, in the normalized distance in the C_{15}–H$\cdots$$C_{13}$ interaction, the contacts are smaller than the sum of the van der Waals radii, so the interaction length in BMP is 2.877 Å, being about 1.1% higher than in BBP. Through the shape index map (Figure 10), it was observed that such an interaction is configured as a C–H $\cdots$ π in both compounds. Finally, it was observed that the C_{17}–H$\cdots$H–C_{18} interaction is formed by contact, whose atomic distances correspond to the van der Waals separation. In BMP, the interaction length is 2391 Å, whereas in BBP this interaction is only 0.76% smaller. The C_5–H$\cdots$$C_{11}$ interaction also occurs in both chalcones. However, the Hirshfeld surfaces showed that the normalized distance for the contacts in this interaction comprises the van der Waals separation. Their lengths in the respective supramolecular arrangements differ by 1.4%, which is greater in BMP.

According to the fingerprint plot (Figure 11), it was observed that the C$\cdots$H and H$\cdots$H contacts are 9.4% and 27.6% larger in BMP supramolecular arrangement, while the C$\cdots$C and O$\cdots$H are 8.3% and 1.5% higher in BBP [8]. Theoretical solubility calculations [https://biosig.lab.uq.edu.au/pkcsm/prediction] (accessed on 14 February 2023) showed that both chalcones are lipid soluble, so the solubility in water, at 25 °C, is in the ratio of 0.96:1, from BMP to BBP. These data showed that the presence of the substituent group –CH3 in the chalcone chain increases the hydrophilicity of BMP, compared to BBP.

The topological parameters obtained by QTAIM showed that the electron density at the bond critical point of each observed interactions is very low ($\rho(\mathbf{r}) < 0.1$ a.u.). The values of these typological parameters are shown in Table 3 and molecular graphs are shown in Figure 12. Through the results, it is possible to observe that the electron densities of C_3–H$\cdots$$O_1$, C_8–H$\cdots$$O_1$, and C_{15}–H$\cdots$$C_{13}$ interactions are 3.6, 4.2, and 4.6 times higher in BMP, respectively. Furthermore, the values obtained for $\nabla^2\rho(\mathbf{r})$ were positive, indicating that the electronic charge is depleted in the BCPs [54]. This indicates that intermolecular interactions are *closed-shell*. The total electronic energy density, $h(\mathbf{r})$, is another topological parameter that helps to characterize the type of interaction in the BCP. The value of $h(\mathbf{r})$ is directly related to $\nabla^2\rho(\mathbf{r})$ through the equation

$$h(\mathbf{r}) = \frac{\hbar^2}{8m}\nabla^2\rho(\mathbf{r}) + \frac{1}{2}v(\mathbf{r}) \quad (13)$$

where $v(\mathbf{r})$ is the local potential energy density[59]. In general, strong interactions present large $\rho(\mathbf{r})$ and $\nabla^2\rho(\mathbf{r})$ and $h(\mathbf{r})$ negative, while in weak interactions, the values of $\rho(\mathbf{r})$ are small and $\nabla^2\rho(\mathbf{r})$ and $h(\mathbf{r})$ are positive. The data presented in Table 3 show that all interactions in BBP resulted in values of $h(\mathbf{r}) > 0$. On the other hand, C_8–H$\cdots$$O_1$, C_{15}–H$\cdots$$C_{13}$, and C_7=$O_1\cdots C_8$ interactions in BMP showed negative values of $h(\mathbf{r})$, and in the other interactions the values are also positive. Based on the results of Nakanishi and coworkers [55,56], we may infer that C_3–H$\cdots$$O_1$ and C_8–H$\cdots$$O_1$ interactions are classified as weak hydrogen bonds in BMP, while they are van der Waals interactions in BBP. The values obtained for the ratio $|v|/G$ indicate that the electron flow in the respective BCPs is very low in these interactions ($|v|/G < 1.0$), except for C_8–H$\cdots$$O_1$, whose value is at the limit, indicating that the electron flow is slightly higher. In both chalcones, C_{17}–H$\cdots$H–C_{18} are classified as van der Waals interactions. In the contact between the A and B rings of BMP, a single bond path was formed, resulting in the C_5–H$\cdots$H–C_{12} interaction, corresponding to C_5–H$\cdots$$C_{12}$. On the other hand, in BBP, the same contact was observed from the bond path that connects the C_5–H portion of the A ring of an asymmetric unit to the C_{11}–C_{12} portion of the B ring of another asymmetric unit. This interaction is similar to a C–H $\cdots$ π interaction. Although it seems redundant to mention the C_8–H$\cdots$$O_1$ and C_7=$O_1\cdots C_8$

interactions, it was observed that in the first one there is the formation of a bonding path between the H and O_1 atoms, while in the second interaction, the bonding path is formed between the C_7=O_1 bond and the C_8 atom, as shown in the molecular graph of BMP. C_7=$O_1 \cdots C_8$ interaction caught our attention due to the topological parameter values found, which indicate that it is a hydrogen bond, despite being a long-distance interaction. The value of the ratio $|v|/G$ indicates that the electron flux is high in the intranuclear region of the interaction, resulting in a partially covalent character ($1.0 < |v|/G < 2.0$).

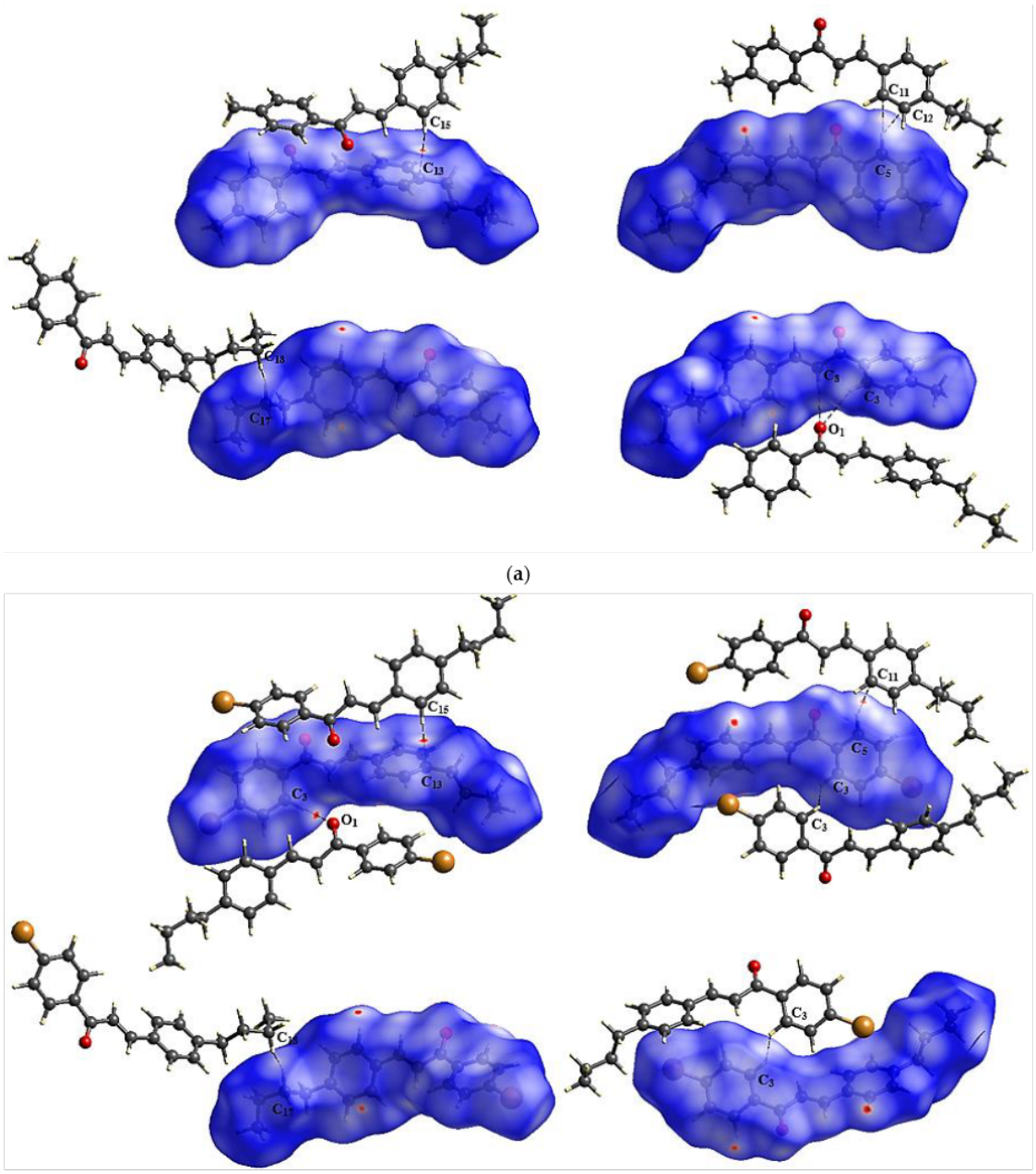

(**a**)

(**b**)

Figure 9. The Hirshfeld surface d_{norm} map showing the interactions observed in the molecular packing of (**a**) BMP and (**b**) BBP chalcones.

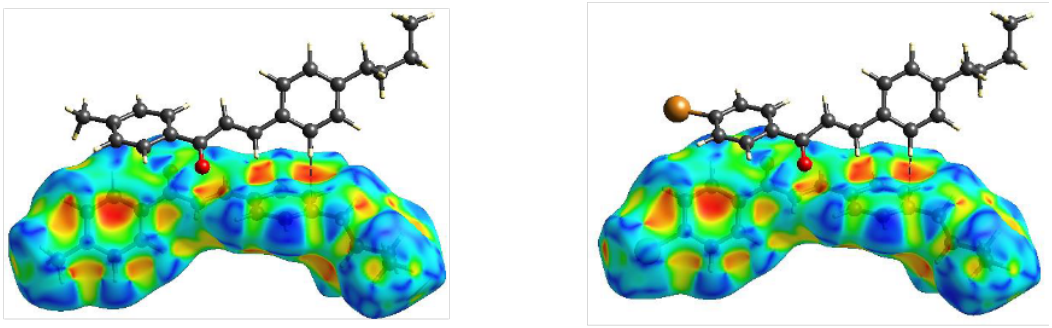

(**a**) (**b**)

Figure 10. Shape index surface showing the C–H···π interactions establishing the crystal packing of (**a**) BMP and (**b**) BBP chalcones.

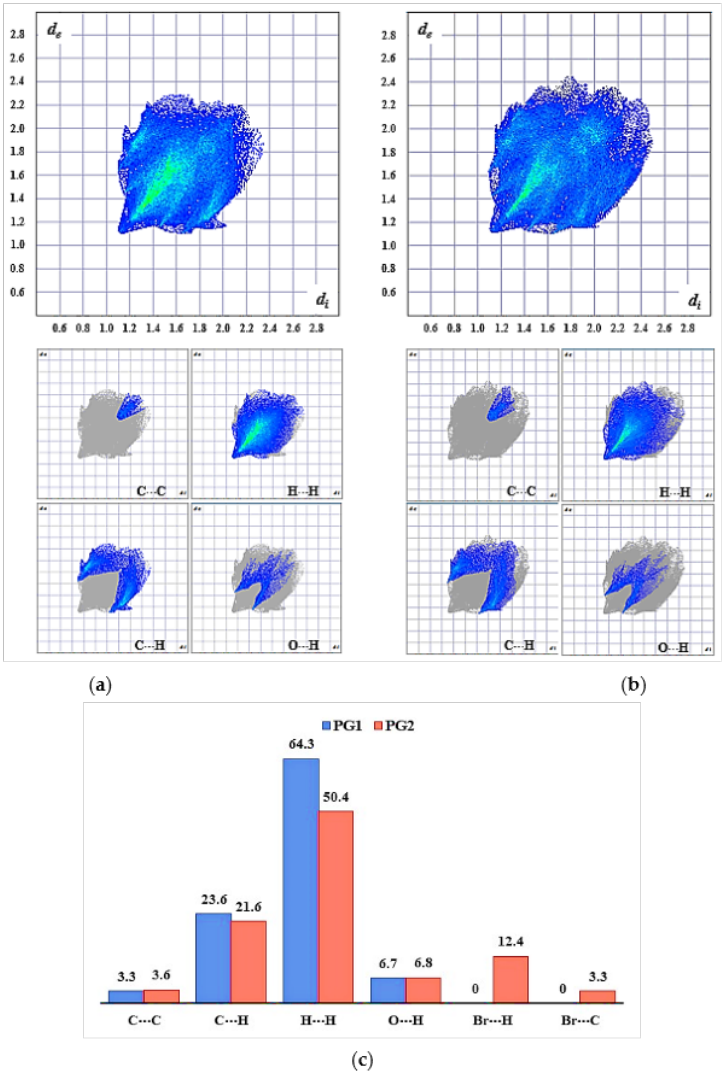

(**a**) (**b**)

(**c**)

Figure 11. 2D fingerprint plots of the nearest external distance (d_e) versus the nearest internal distance (d_i) for (**a**) BMP and (**b**) BBP chalcones, and the regions corresponding to C···C, C···H, H···H, O···H, Br···H, and Br···C contacts. The colors represent the number of points that share the same d_i, d_e coordinate (light blue: many; dark blue: few). (**c**) Graph of the percentages of each contact on the Hirshfeld surface in the BMP (blue) and BBP (red) chalcones.

Table 3. Hydrogen-bond geometry and topological parameters calculated for the BMP and BBP molecular interactions at the bond critical point.

Interaction	H···A (Å)	D–H···A (°)	ρ_{BCP} [a] (a.u.)	$\nabla^2\rho_{BCP}$ [b] (a.u.)	G(r) [c] (a.u.)	v(r) [d] (a.u.)	h(r) [e] (a.u.)	$\frac{\lvert v(r)\rvert}{G(r)}$
BMP								
C_3–H···O_1	2.753	148.44	0.0219	0.0504	0.0107	−0.0089	0.0019	0.8
C_8–H···O_1	2.767	158.31	0.0194	0.0217	0.0060	−0.0066	−0.0006	1.1
C_{15}–H···C_{13}	2.877	148.87	0.0264	0.0388	0.0121	−0.0144	−0.0024	1.2
C_5–H···C_{11}	2.884	138.40	-	-	-	-	-	-
C_5–H···C_{12}	2.886	121.22	0.0215	0.0314	0.0078	−0.0078	0.0000	1.0
C_{17}–H···H–C_{18}	2.391	140.07	0.0048	0.0179	0.0034	−0.0022	0.0011	0.7
C_7=O_1···C_8	3.467	85.93	0.0286	0.0040	0.0033	−0.0056	−0.0023	1.7
BBP								
C_3–H···O_1	2.666	147.47	0.0060	0.0202	0.0043	−0.0035	0.0008	0.8
C_8–H···O_1	2.723	157.43	0.0046	0.0166	0.0035	−0.0028	0.0007	0.8
C_{15}–H···C_{13}	2.846	146.19	0.0058	0.0160	0.0034	−0.0028	0.0006	0.8
C_5–H···C_{11}	2.845	135.33	0.0058	0.0184	0.0037	−0.0028	0.0009	0.8
C_{17}–H···H–C_{18}	2.373	140.37	0.0051	0.0149	0.0032	−0.0027	0.0005	0.8
C_{11}–H···O_1	2.929	140.32	0.0039	0.0134	0.0028	−0.0022	0.0006	0.8
C_3–H···H–C_3	2.397	120.68	0.0054	0.0178	0.0036	−0.0028	0.0008	0.8

[a] Total electronic density on BCP; [b] Laplacian of electron density on BCP; [c] Lagrangian Kinect energy; [d] Potential energy density; [e] Total energy density.

Tables S1 and S2 (supplementary material) contain the NBOs data for the interactions observed in BMP and BBP. NBO analysis showed that the C_3–H···O_1 interactions in both chalcones are formed from low values of stabilizing energies. However, the number of hyperconjugations between the donor orbital (Lewis type) and the acceptor orbital (non-Lewis type) differs in each compound, being higher in BMP. The orbital of the O_1 lone pair, $\eta_1(O_1)$, hyperconjugates with the antibonding σ^* orbital of the C_3–H bond, where the value of $E^{(2)}$ is about 70.1% lower in BMP. The occupancy of the $\eta_1(O_1)$ orbital is 1.98*e*, so the O_1 atom is a hybrid $sp^{0.74}$ in BMP and $sp^{0.75}$ in BBP. The occupancy of the antibonding σ^* orbital of C_3–H is 0.012*e*, where in BMP it is formed by the contribution of 40.7% of the $sp^{2,11}$ hybrid orbital of C_3 and 59.3% of the s orbital of H, while in BBP it is formed by the contribution of 40.1% of the $sp^{2,14}$ hybrid orbital of C_3 and 59.9% of the *s* orbital of H. However, the formation of this bond, in BMP, also occurs by the hyperconjugations $\eta_1(O_1) \rightarrow \sigma^*(C_3–H)$, $\sigma(C_3–H) \rightarrow \sigma^*(C_7–O_1)$ and $\sigma(C_3–H) \rightarrow \pi^*(C_7–O_1)$, while in BBP, also by the hyperconjugation $\eta_1(O_1) \rightarrow \sigma^*(C_3–C_4)$. In other words, the greater number of hyperconjugations that form the C_3–H···O_1 interaction makes it more stable in BMP compared to BBP. The hyperconjugation $\sigma(C_3–H) \rightarrow \pi^*(C_7–O_1)$ in BMP presented a value of $E^{(2)}$ = 12.02 kcal/mol, indicating that the interaction presents greater stability.

In the case of the C_8–H···O_1 interaction, we observed that the bonding s orbital of the C_8–C_9 bond hyperconjugates with the antibonding π^* orbital of the C_7=O_1 bond in BMP and the π orbital bonding the C_8–C_9 bond with the orbital π^* antibonding of the C_7=O_1 bond on BBP. In both cases, the $E^{(2)}$ value is 0.16 kcal/mol. In BMP, the bonding σ orbital, $\sigma(C_8–C_9)$, has an occupancy equal to 1.98*e*, being formed by 50.15% of the $sp^{1.75}$ hybrid orbital of C_8 and 49.85% of the $sp^{1.76}$ hybrid orbital of C_9 and the antibonding π^* orbital has an occupancy of 0.18*e*, being formed by the contribution of 68.34% and 31.66% of the *p* orbitals of the respective C_7 and O_1 atoms. In BBP, the occupancy of the bonding π orbital is 1.86*e*, being formed by 54.66% and 45.34% of the pure *p* orbitals of C_8 and C_9 atoms, respectively, while the antibonding π^* orbital is formed by 67.98% and 32.02% of the *p* orbitals of atoms C_7 and O_1. Furthermore, we observed that, in BBP, there is an extra hyperconjugation that contributes to the stabilization of this interaction, $\pi(C_7–O_1) \rightarrow \pi^*(C_8–C_9)$, with a value of $E^{(2)}$ = 0.06 kcal/mol. The C_7=O_1···C_8 interaction observed

in the QTAIM results in BMP is formed by the same hyperconjugation as the C_8–H$\cdots O_1$ interaction, i.e., $\sigma(C_8–C_9) \rightarrow \pi^*(C_7–O_1)$.

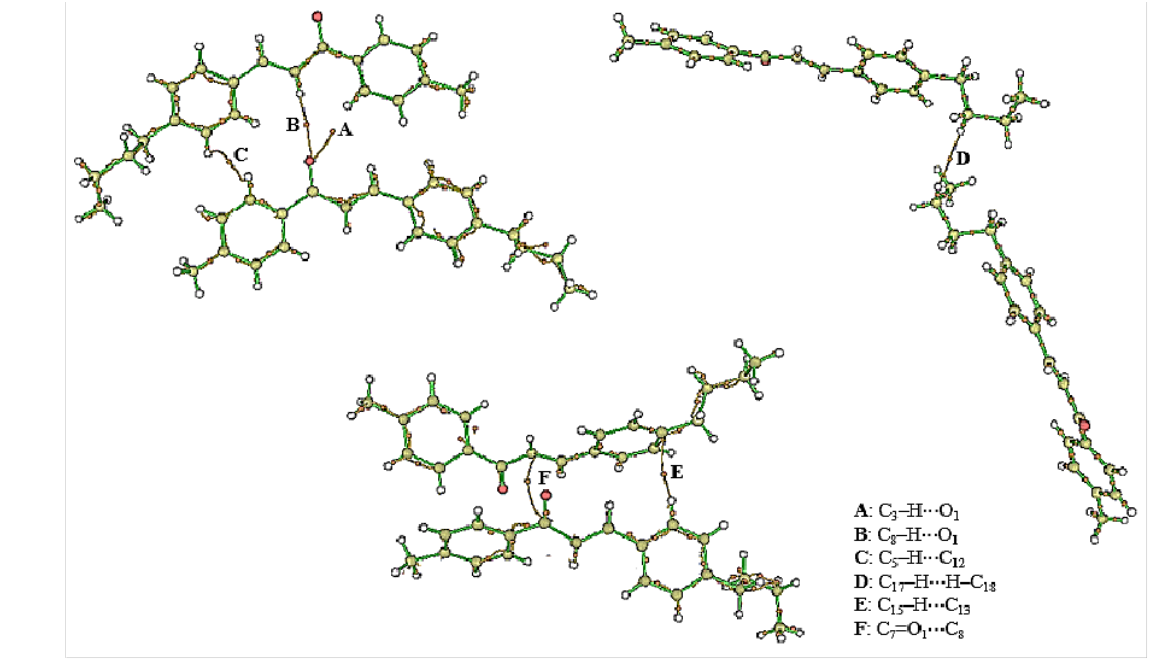

(**a**)

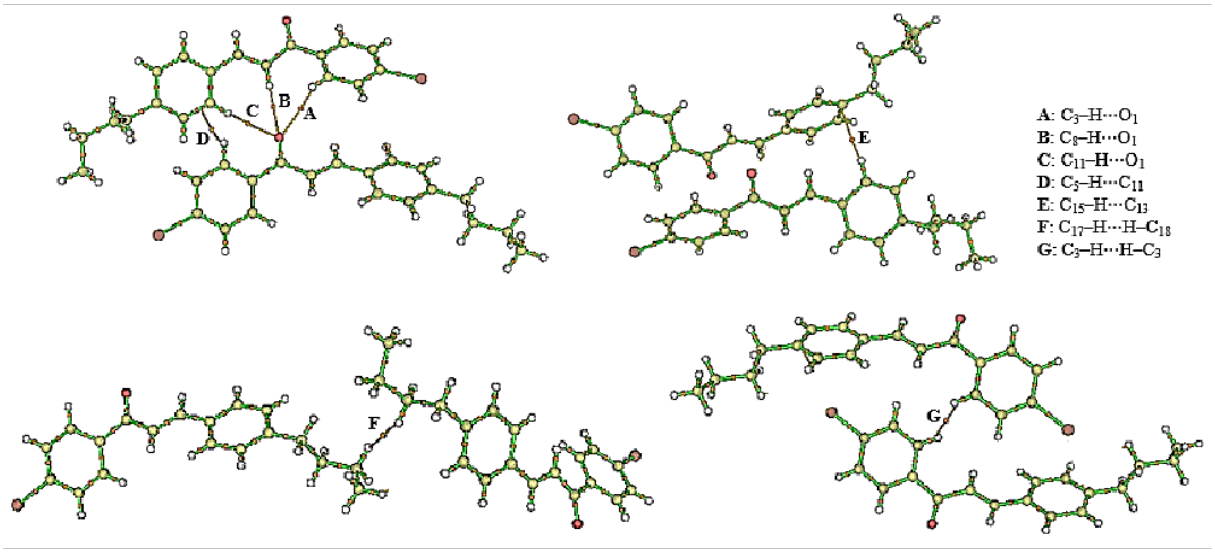

(**b**)

Figure 12. Molecular graphs of some bond paths of the intermolecular interactions in the supramolecular arrangements of the (**a**) BMP and (**b**) BBP chalcones.

The C_{17}–H$\cdots$H–C_{18} interaction in BMP was shown to be 11 times more stable in BMP compared to BBP. In both compounds, $\sigma(C_{17}–H) \rightarrow \sigma^*(C_{18}–H)$ hyperconjugation was observed, in which the values obtained for $E^{(2)}$ were, respectively, 17.78 and 1.61 kcal/mol. The $\sigma(C_{17}–H)$ orbitals have an occupancy of 1.98*e*. In BMP, this orbital is formed by 60.44% of the $sp^{2.91}$ hybrid orbital of C_{17} with 39.56% of the *s* orbital of H, while in BBP, it is formed by 59.17% of the $sp^{3.11}$ hybrid orbital of C_{17} with 40.83% of the *s* orbital of H. The $\sigma^*(C_{18}–H)$ orbital in BMP has an occupancy of 0.011*e* and is formed by the contribution of 39.73% of

the $sp^{2.97}$ hybrid orbital of C_{18} with 60.27% of the *s* orbital of H, while in BBP, its occupancy is 0.014*e*, being formed by 41.15% of the $sp^{3,19}$ hybrid orbital of C_{18} with 58.85% of the *s* orbital of H. Other hyperconjugations were observed in BMP, such as $\sigma(C_{16}–C_{17}) \rightarrow \sigma^*(C_{18}–H)$, $\sigma(C_{18}–H) \rightarrow \sigma^*(C_{17}–H)$, and $\sigma(C_{18}–C_{19}) \rightarrow \sigma^*(C_{17}–H)$, all with low $E^{(2)}$ values (0.11, 0.32, and 0.48 kcal/mol, respectively). In BBP, only the extra $\sigma(C_{17}–H) \rightarrow \sigma^*(C_{17}–C_{18})$ hyperconjugation was observed, with $E^{(2)}$ value equal to 0.28 kcal/mol.

It was observed that eight hyperconjugations stabilize the $C_5–H\cdots C_{11}$ interaction in BMP, while in BBP, only three. In BMP, $\sigma(C_5–H) \rightarrow \sigma^*(C_{10}–C_{11})$ hyperconjugation occurs, with $E^{(2)}$ = 0.06 kcal/mol, and in BBP, hyperconjugation of the same ligand σ orbital occurs with the antibonding π^* orbital of the $C_{10}–C_{11}$ bond, $\sigma(C_5–H) \rightarrow \pi^*(C_{10}–C_{11})$, with $E^{(2)}$ = 0.10 kcal/mol. In both compounds, the $\sigma(C_5–H)$ orbital has an occupancy of 1.98*e*. However, the acceptor orbitals are formed by different contributions, since they are different orbitals in the chalcones. In BMP, this orbital is formed by 59.41% of the $sp^{2.08}$ hybrid orbital of C_5 and 40.59% of the *s* orbital of H. In BBP, it is formed by the contribution of 60.07% of the $sp^{2,11}$ hybrid orbital of C_5 and 39.93% of the *s* orbital of H. In the case of the acceptor orbital, in BMP, $\sigma^*(C_{10}–C_{11})$ is formed by 49.39% of the $sp^{1.96}$ hybrid orbital of C_{10} and 50.66% of the $sp^{1,96}$ hybrid orbital of C_{11}, while in BBP the $\pi^*(C_{10}–C_{11})$ orbital is formed by 47.59% and 52.41% of pure *p* orbitals of C_{10} and C_{11}, respectively. The hyperconjugations that best contribute to the stabilization of the $C_5–H\cdots C_{11}$ interaction in BMP are σ (C_5–C6) $\rightarrow \pi^*(C_{11}–C_{12})$, with $E^{(2)}$ = 5.72 kcal/mol, followed by $\pi(C_{11}–C_{12}) \rightarrow \sigma^*(C_5–H)$, where $E^{(2)}$ = 1.83 kcal/mol.

In BBP, two hyperconjugations contribute to the stabilization of the $C_3–H\cdots H–C_3$ interaction: $\sigma(C_3–H) \rightarrow \sigma^*(C_3–H)$, with $E^{(2)}$ = 0.11 kcal/mol, and $\pi(C_3–C_4) \rightarrow \sigma^*(C_3–H)$, with $E^{(2)}$ = 0.06 kcal/mol. The $\sigma(C_3–H)$ donor orbital is formed by 59.18% of the $sp^{2,17}$ hybrid of C_3 and 40.82% of the *s* orbital of H and has an occupancy of 1.98*e*. The donor $\pi(C_3–C_4)$ orbital is formed by 47.96% and 52.04% of the pure *p* orbitals of atoms C_3 and C_4, respectively, and its occupancy is 1.65*e*. The acceptor orbital is formed by 40.82% of the $sp^{2,17}$ hybrid orbital of C_3 and 59.18% of the *s* orbital of H, whose occupancy is 0.012*e*. We take the hyperconjugations with the most considerable values of hyperconjugation energies that stabilize the interactions observed in the supramolecular arrangements of the studied chalcones. However, other hyperconjugations are shown in Tables S1 and S2 of the supplementary material.

3.4. Analysis of Photoprotective Property

The experimental UV-vis spectra (Figure 13a,c) showed that BMP and BBP molecules have an absorption band in the range of 300–350 nm, with this absorption range being typical of chalcones [5,18]. This absorption range can be attributed to $\pi \rightarrow \pi$ transitions, which are similar to chalcone-type molecules [57,58]. The maximum wavelengths, λ_{max}, obtained were 308 and 331 nm, respectively. The sunscreen agents are classified according to the range wavelength of protection: UV-B (290–320 nm) and UV-A (320–400 nm), and broad-spectrum (290–400 nm). In this regard, according to their UV-vis spectra, the BMP and BBP appear to be promising organic sunscreen agent candidates as an alternative to *p*-aminobenzoic acid (PABA), ethylhexylmethoxycinnamate derivatives, and others [59].

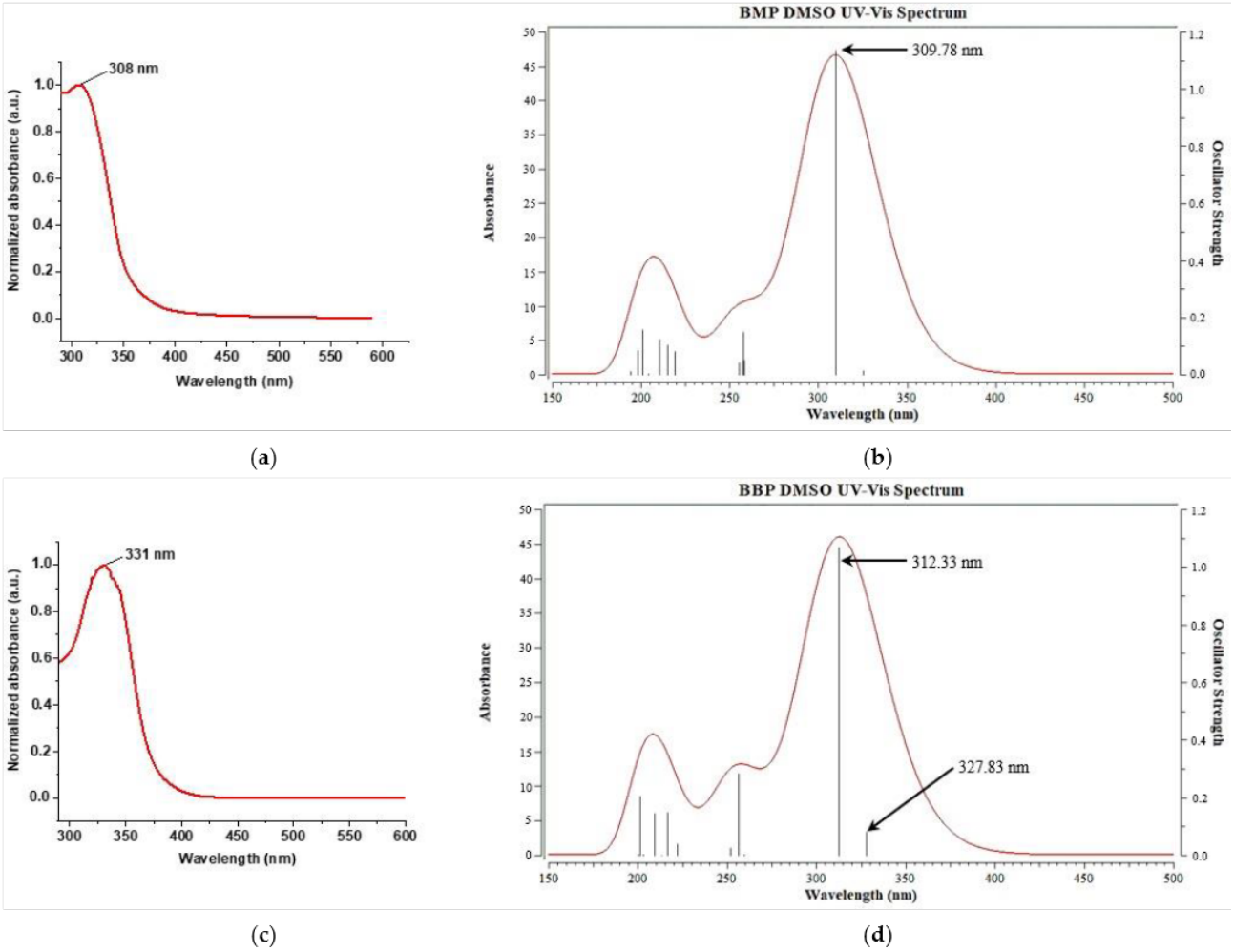

Figure 13. UV-vis spectra (**a**,**b**) experimental and (**c**,**d**) theoretical of BMP, and BBP chalcones in DMSO.

The BMP theoretical UV-vis spectrum (Figure 13b) showed absorption in the same range so the λ_{max} value is only 0.6% displaced from the experimental one. For this value, we observed a single electronic transition (H→L) that occurs in the second excited state (S_2). The vertical excited energy (Table 4) required for this transition is 92.3 kcal/mol and the oscillator strength is 1.1349, so it contributes 90.45% in that state. This electronic transition is characterized as π→π*, contributing to 90.45% of the transitions in this excited state. For the BBP UV-vis spectrum, two excited states were observed. The first, corresponding to the S_1 state, appears at 327.83 nm and has vertical excited energy of 87.2 kcal/mol. This is displaced from the experimental λ_{max} by 0.4%. However, the oscillator strength is only 0.0805. In this excited state, four electronic transitions were observed, H-4→L, H-3→L, H→L, and H-1→L, with the first contribution of 62.58%. The second excited state (S2) appears at 312.33 nm, with vertical excited energy of 91.5 kcal/mol, being displaced 5.6% from the experimental λ_{max}. However, the strength of the oscillator is 1.0669. In this state, four electronic transitions were also observed, with H→L presenting the highest contribution. All electronic transitions cited for BBP are characterized as π→π*.

Table 4. Vertical excitation energies (*E*), absorption wavelength (λ), oscillator strength (*f*) and the corresponding electronic transition of the twelve excited states of BMP and BBP calculated by TD-DFT/CAM-B3LYP/6-311++G(d,p) level of theory in DMSO.

Excited State	*E* (kcal/mol)	λ^{theor} (nm)	λ^{exper} (nm)	*f*	Excitation	Transition	%
			BMP				
S_1	87.878	325.36		0.0148	H–4 → L	$\sigma \rightarrow \pi^*$	80.03
S_2	92.299	309.78	308	1.1349	H → L	$\pi \rightarrow \pi^*$	90.45
S_3	110.757	258.15		0.0506	H–2 → L	$\pi \rightarrow \pi^*$	36.6
					H–1 → L	$\pi \rightarrow \pi^*$	32.81
					H → L + 5	$\pi \rightarrow \pi^*$	13.94
S_4	111.075	257.41		0.1487	H–1 → L	$\pi \rightarrow \pi^*$	49.6
					H–2 → L	$\pi \rightarrow \pi^*$	25.01
S_5	111.947	255.41		0.0419	H–3 → L	$\pi \rightarrow \pi^*$	65.58
					H–3 → L + 1	$\pi \rightarrow \pi^*$	12.06
					H–1 → L + 4	$\pi \rightarrow \pi^*$	11.68
S_6	130.488	219.12		0.0812	H → L + 1	$\pi \rightarrow \pi^*$	45.77
					H → L + 5	$\pi \rightarrow \pi^*$	22.32
					H–2 → L	$\pi \rightarrow \pi^*$	15.32
S_7	133.024	214.94	214	0.1035	H → L + 5	$\pi \rightarrow \pi^*$	41.96
					H → L + 1	$\pi \rightarrow \pi^*$	22.58
					H–2 → L	$\pi \rightarrow \pi^*$	13.85
S_8	136.039	210.17		0.1243	H–1 → L + 4	$\pi \rightarrow \pi^*$	38.8
					H-3 → L	$\pi \rightarrow \pi^*$	25.35
					H–1 → L + 1	$\pi \rightarrow \pi^*$	11.57
S_9	140.109	204.07		0.0024	H → L + 2	$\pi \rightarrow \sigma^*$	60.69
S_{10}	142.413	200.77		0.1578	H–1 → L + 1	$\pi \rightarrow \pi^*$	26.2
					H–3 → L + 4	$\pi \rightarrow \pi^*$	23.39
S_{11}	144.223	198.25		0.0848	H–5 → L	$\pi \rightarrow \pi^*$	49.33
S_{12}	147.428	193.94		0.0118	H–4 → L + 1	$\sigma \rightarrow \pi^*$	67.71
			BBP				
S_1	87.216	327.83	331	0.0805	H–4 → L	$\pi \rightarrow \pi^*$	62.58
					H–3 → L	$\pi \rightarrow \pi^*$	13.56
					H → L	$\pi \rightarrow \pi^*$	11.61
S_2	91.545	312.33		1.0669	H → L	$\pi \rightarrow \pi^*$	80.49
S_3	110.162	259.55		0.0039	H–2 → L	$\pi \rightarrow \pi^*$	61.74
S_4	111.439	256.57		0.2825	H–1 → L	$\pi \rightarrow \pi^*$	81.83
S_5	113.612	251.66		0.0264	H–3 → L	$\pi \rightarrow \pi^*$	50.84
					H–1 → L + 2	$\pi \rightarrow \pi^*$	16.85
					H–4 → L	$\pi \rightarrow \pi^*$	11.39
					H–3 → L + 1	$\pi \rightarrow \pi^*$	11.03
S_6	128.744	222.08		0.038	H → L + 1	$\pi \rightarrow \pi^*$	61.96
S_7	132.137	216.38		0.1495	H → L + 6	$\pi \rightarrow \sigma^*$	51.22
					H–2 → L	$\pi \rightarrow \pi^*$	20.01
					H → L + 1	$\pi \rightarrow \pi^*$	11.13
S_8	134.069	213.26	213	0.0007	H–1 → L + 6	$\pi \rightarrow \sigma^*$	44.9
					H–1 → L + 2	$\pi \rightarrow \pi^*$	11.49
S_9	136.592	209.32		0.1464	H–1 → L + 2	$\pi \rightarrow \pi^*$	43.55
					H–3 → L	$\pi \rightarrow \pi^*$	26.25
S_{10}	140.725	203.18		0.0034	H → L + 2	$\pi \rightarrow \pi^*$	55.62
					H → L + 8	$\pi \rightarrow \sigma^*$	19.42
S_{11}	142.182	201.09		0.2044	H–6 → L	$\pi \rightarrow \pi^*$	58.15
					H → L + 1	$\pi \rightarrow \pi^*$	11.05
S_{12}	142.855	200.15		0.0016	H–1 → L + 1	$\pi \rightarrow \pi^*$	45.17
					H–3 → L + 2	$\pi \rightarrow \pi^*$	14.57

4. Conclusions

Aiming to produce potential photoprotective agents, the butylchalcone derivative BMP was synthetized and fully characterized by UV-vis, Raman, IR, ^{1}H-, and ^{13}C-NMR

spectroscopies, DSC analysis, and mass spectrometry (MS). Moreover, its structural description was performed by X-ray diffraction. A comparative analysis was performed for the two chalcones bearing methyl (BMP) and bromo (BBP) substituent groups (at *para* position) on the molecular and electronic structures, and on the supramolecular arrangement through DFT. Both butylchalcone derivatives are in the same space group (Pbca), and the substituent groups do not significantly change their molecular conformations. Although BMP is slightly more stable than BBP, the chemical reactivity descriptors obtained showed that the molecules are electronically similar. Furthermore, the intermolecular interactions patterns in the supramolecular arrangement are very similar, containing mostly van der Waals interactions and weak hydrogen bonds. NBO analysis showed that all interactions are weakly hyperconjugated, giving little stability. The Fukui indices pointed out the regions where possible radical attacks can happen in both chalcones, and the spin density calculations showed the probability densities in these regions. The calculations showed that the formed radicals have low stability, but BMP and BBP are potential antioxidant agents. The UV-vis spectra showed that both chalcones also have potential as organic sunscreens due to the presence of chromophores, associated with *p* electrons along their entire carbon chain, in addition to being capable of absorbing radiation in the UVA and UVB range. Additionally, regarding the structure–activity relationship of the chalcones (BMP and BBP) with phototoprotective property, the C-4 butyl chain was chosen as a starting point for molecular modeling evaluation (X-ray, spectroscopy characterization, theoretical studies). Moreover, aiming to evaluate and modulate the UV-vis absorption profile (a pivotal property for sunscreen agent), two substituent groups, $-CH_3$ (electron-donating) and –Br (electron-withdrawing), at para position on the aromatic ring were studied. These structural modifications resulted in a change in UV-vis absorption of the chalcones, which can be explored further. As a future perspective, both chalcones (BMP and BBP) could be added as organic photoprotective agents in topical sunscreens formulations or in combination with inorganic photoprotective agents, such as titanium dioxide and zinc oxide [60], in order to improve the efficiency of the commercial sunscreens.

Supplementary Materials: The following supporting information can be downloaded at: https://www.mdpi.com/article/10.3390/photonics10030228/s1, Figure S1. UV-vis spectrum of BMP in DMSO; Figure S2. Raman spectrum BMP crystal. Raman peak at 640 cm^{-1} was used to normalize the spectrum; Figure S3. ^{1}H-NMR spectrum of BMP; Figure S4. ^{13}C-NMR spectrum of BMP; Figure S5. DSC analysis of BMP; Figure S6. MS spectrum of BMP; Figure S7. IR spectrum of BMP; Figure S8: Bond angle between the rings A and B from (a) BMP e (b) BBP; Table S1: Second-order perturba-tion theory analysis in NBO basis obtained at M06-2X/6-311++G(d,p) level of theory for the BMP and BBP chalcones; Table S2: Second-order perturbation theory analysis in NBO basis obtained at M06-2X/6-311++G(d,p) level of theory for the BMP chalcone; Table S3: Second-order perturbation theory analysis in NBO basis obtained at M06-2X/6-311++G(d,p) level of theory for the BBP chalcone.

Author Contributions: Conceptualization, A.S.N.A., L.D.D., G.L.B.A., A.J.C. and H.B.N.; methodology, A.S.N.A., P.G.M.D., G.L.B.A., A.J.C. and H.B.N.; software, A.J.C. and H.B.N.; validation, L.D.D., G.L.B.A., A.J.C. and H.B.N.; formal analysis, A.S.N.A., P.G.M.D., J.E.Q., P.P.F., J.M.F.C., L.D.D., G.L.B.A., A.J.C. and H.B.N.; investigation, A.S.N.A., P.G.M.D., J.E.Q., P.P.F., J.M.F.C., L.D.D., G.L.B.A., A.J.C. and H.B.N.; data curation, A.S.N.A., G.L.B.A., A.J.C. and H.B.N.; writing—original draft preparation, A.S.N.A., P.G.M.D., L.D.D., G.L.B.A., A.J.C. and H.B.N.; writing—review and editing, A.S.N.A., P.G.M.D., J.E.Q., P.P.F., J.M.F.C., L.D.D., G.L.B.A., A.J.C. and H.B.N.; supervision, A.S.N.A., L.D.D., G.L.B.A., A.J.C. and H.B.N.; project administration, L.D.D., G.L.B.A., A.J.C. and H.B.N.; funding acquisition, L.D.D., G.L.B.A., A.J.C. and H.B.N. All authors have read and agreed to the published version of the manuscript.

Funding: The authors are grateful to Coordenação de Aperfeiçoamento de Pessoal de Nível Superior (CAPES), Conselho Nacional de Desenvolvimento Científico e Tecnológico (CNPq) and Fundação de Amparo à Pesquisa de Goiás (FAPEG). Theoretical calculations were carried out in the High-Performance Computing Center of the Universidade Estadual de Goiás. L. D. Dias thanks Conselho Nacional de Desenvolvimento Científico e Tecnológico (CNPq) for his Post-doc grant 151188/2022-0. J.E.Q. thanks Coordenação de Aperfeiçoamento de Pessoal de Nível Superior (CAPES) for her doctoral grant (88887.486017/2020-00) and P.P Firmino thanks to CNPq 160856/2021-3.

Data Availability Statement: Data is contained within the article or supplementary material.

Conflicts of Interest: The authors declare no conflict of interest.

References

1. Wang, S.Q.; Balagula, Y.; Osterwalder, U. Photoprotection: A Review of the Current and Future Technologies. *Dermatol. Ther.* **2010**, *23*, 31–47. [CrossRef] [PubMed]
2. Afaq, F. Natural agents: Cellular and molecular mechanisms of photoprotection. *Arch. Biochem. Biophys.* **2011**, *508*, 144–151. [CrossRef] [PubMed]
3. Saewan, N.; Jimtaisong, A. Natural products as photoprotection. *J. Cosmet. Dermatol.* **2015**, *14*, 47–63. [CrossRef] [PubMed]
4. Gregoris, E.; Fabris, S.; Bertelle, M.; Grassato, L.; Stevanato, R. Propolis as potential cosmeceutical sunscreen agent for its combined photoprotective and antioxidant properties. *Int. J. Pharm.* **2011**, *405*, 97–101. [CrossRef]
5. Wijayanti, L.W.; Swasono, R.T.; Lee, W.; Jumina, J. Synthesis and Evaluation of Chalcone Derivatives as Novel Sunscreen Agent. *Molecules* **2021**, *26*, 2698. [CrossRef]
6. Lahsasni, S.A.; Al Korbi, F.H.; Aljaber, N.A.A. Synthesis, characterization and evaluation of antioxidant activities of some novel chalcones analogues. *Chem. Cent. J.* **2014**, *8*, 32. [CrossRef]
7. Kozlowska, J.; Potaniec, B.; Baczynska, D.; Zarowska, B.; Aniol, M. Synthesis and Biological Evaluation of Novel Aminochalcones as Potential Anticancer and Antimicrobial Agents. *Molecules* **2019**, *24*, 4129. [CrossRef]
8. Rocha, S.; Ribeiro, D.; Fernandes, E.; Freitas, M. A Systematic Review on Anti-diabetic Properties of Chalcones. *Curr. Med. Chem.* **2020**, *27*, 2257–2321. [CrossRef]
9. Targanski, S.K.; Sousa, J.R.; de Padua, G.M.S.; de Sousa, J.M.; Vieira, L.C.C.; Soares, M.A. Larvicidal activity of substituted chalcones against *Aedes aegypti* (Diptera: Culicidae) and non-target organisms. *Pest Manag. Sci.* **2021**, *77*, 325–334. [CrossRef]
10. Kozlowska, J.; Potaniec, B.; Zarowska, B.; Aniol, M. Microbial transformations of 4-methylchalcones as an efficient method of obtaining novel alcohol and dihydrochalcone derivatives with antimicrobial activity. *RSC Adv.* **2018**, *8*, 30379–30386. [CrossRef]
11. Roussaki, M.; Hall, B.; Lima, S.C.; da Silva, A.C.; Wilkinson, S.; Detsi, A. Synthesis and anti-parasitic activity of a novel quinolinone-chalcone series. *Bioorganic Med. Chem. Lett.* **2013**, *23*, 6436–6441. [CrossRef]
12. Herencia, F.; Ferrandiz, M.L.; Ubeda, A.; Dominguez, J.N.; Charris, J.E.; Lobo, G.M.; Alcaraz, M.J. Synthesis and anti-inflammatory activity of chalcone derivatives. *Bioorganic Med. Chem. Lett.* **1998**, *8*, 1169–1174. [CrossRef]
13. Sooknual, P.; Pingaew, R.; Phopin, K.; Ruankham, W.; Prachayasittikul, S.; Ruchirawat, S.; Prachayasittikul, V. Synthesis and neuroprotective effects of novel chalcone-triazole hybrids. *Bioorganic Chem.* **2020**, *105*, 104384. [CrossRef]
14. Gaonkar, S.L.; Vignesh, U.N. Synthesis and pharmacological properties of chalcones: A review. *Res. Chem. Intermed.* **2017**, *43*, 6043–6077. [CrossRef]
15. Custodio, J.M.F.; Guimaraes-Neto, J.J.A.; Awad, R.; Queiroz, J.E.; Verde, G.M.V.; Mottin, M.; Neves, B.J.; Andrade, C.H.; Aquino, G.L.B.; Valverde, C.; et al. Molecular modelling and optical properties of a novel fluorinated chalcone. *Arab. J. Chem.* **2020**, *13*, 3362–3371. [CrossRef]
16. Custodio, J.M.F.; Moreira, C.A.; Valverde, C.; de Aquino, G.L.B.; Baseia, B.; Napolitano, H.B. Hirshfeld Surfaces and Nonlinear Optics on Two Conformers of a Heterocyclic Chalcone. *J. Braz. Chem. Soc.* **2018**, *29*, 258–268. [CrossRef]
17. Borges, I.D.; Danielli, J.A.V.; Silva, V.E.G.; Sallum, L.O.; de Queiroz, J.E.; Dias, L.D.; Iermak, I.; Aquino, G.L.B.; Camargo, A.J.; Valverde, C.; et al. Synthesis and structural studies on (E)-3-(2,6-difluorophenyl)-1-(4-fluorophenyl)prop-2-en-1-one: A promising nonlinear optical material. *RSC Adv.* **2020**, *10*, 22542–22555. [CrossRef] [PubMed]
18. Fatmasari, E.; Zulkarnain, A.K.; Kuswahyuning, R. 3,4-dimethoxychalcone novel ultraviolet-A-protection factor in conventional sunscreen cream. *J. Adv. Pharm. Technol. Res.* **2021**, *12*, 279–284. [CrossRef]
19. Fayed, T.A.; Gaber, M.; El-Nahass, M.N.; Diab, H.A.; El-Gamil, M.M. Synthesis, Structural characterization, thermal, molecular modeling and biological studies of chalcone and Cr(III), Mn(II), Cu(II) Zn(II) and Cd(II) chelates. *J. Mol. Struct.* **2020**, *1221*, 128742. [CrossRef]
20. Carvalho, P.S.; Sallum, L.O.; Cidade, A.F.; Aquino, G.L.B.; Napolitano, H.B. (E)-1-(4-Methoxyphenyl)-3-(3,4,5-trimethoxyphenyl) prop-2-en-1-one. *Acta Crystallogr. Sect. E-Struct. Rep. Online* **2011**, *67*, O2126–U1337. [CrossRef]
21. Firmino, P.P.; Queiroz, J.E.; Dias, L.D.; Wenceslau, P.R.S.; de Souza, L.M.; Iermak, I.; Vaz, W.F.; Custodio, J.M.F.; Oliver, A.G.; de Aquino, G.L.B.; et al. Synthesis, Molecular Structure, Thermal and Spectroscopic Analysis of a Novel Bromochalcone Derivative with Larvicidal Activity. *Crystals* **2022**, *12*, 440. [CrossRef]
22. Sheldrick, G.M. A short history of SHELX. *Acta Crystallogr. Found. Adv.* **2008**, *64*, 112–122. [CrossRef]

23. Dolomanov, O.V.; Bourhis, L.J.; Gildea, R.J.; Howard, J.A.K.; Puschmann, H. OLEX2: A complete structure solution, refinement and analysis program. *J. Appl. Crystallogr.* **2009**, *42*, 339–341. [CrossRef]
24. Sheldrick, G.M. Crystal structure refinement with SHELXL. *Acta Crystallogr. Sect. C-Struct. Chem.* **2015**, *71*, 3–8. [CrossRef] [PubMed]
25. Spek, A.L. Structure validation in chemical crystallography. *Acta Crystallogr. Sect. D-Struct. Biol.* **2009**, *65*, 148–155. [CrossRef] [PubMed]
26. Spackman, P.R.; Turner, M.J.; McKinnon, J.J.; Wolff, S.K.; Grimwood, D.J.; Jayatilaka, D.; Spackman, M.A. CrystalExplorer: A program for Hirshfeld surface analysis, visualization and quantitative analysis of molecular crystals. *J. Appl. Crystallogr.* **2021**, *54*, 1006–1011. [CrossRef]
27. Hohenberg, P.; Kohn, W. Inhomogeneous electron gas. *Phys. Rev. B* **1964**, *136*, B864. [CrossRef]
28. Kohn, W.; Sham, L.J. Self-consistent equations including exchange and correlation effects. *Phys. Rev.* **1965**, *140*, 1133. [CrossRef]
29. Frisch, M.J.; Trucks, G.W.; Schlegel, H.B.; Scuseria, G.E.; Robb, M.A.; Cheeseman, J.R.; Scalmani, G.; Barone, V.; Petersson, G.A.; Nakatsuji, H.; et al. *Gaussian 16, Revision C.01*; Gaussian, Inc.: Wallingford, CT, USA, 2016.
30. Zhao, Y.; Truhlar, D.G. The M06 suite of density functionals for main group thermochemistry, thermochemical kinetics, noncovalent interactions, excited states, and transition elements: Two new functionals and systematic testing of four M06-class functionals and 12 other functionals. *Theor. Chem. Acc.* **2008**, *120*, 215–241. [CrossRef]
31. Zhang, G.; Musgrave, C.B. Comparison of DFT methods for molecular orbital eigenvalue calculations. *J. Phys. Chem. A* **2007**, *111*, 1554–1561. [CrossRef]
32. Narayszabo, G.; Ferenczy, G.G. Molecular electrostatics. *Chem. Rev.* **1995**, *95*, 829–847. [CrossRef]
33. Fukui, K. The role of frontier orbitals in chemical-reactions (nobel lecture). *Angew. Chem.-Int.* **1982**, *21*, 801–809. [CrossRef]
34. Fukui, K. Role of frontier orbitals in chemical-reactions. *Science* **1982**, *218*, 747–754. [CrossRef] [PubMed]
35. Overhauser, A.W. Spin density waves in an electron gas. *Phys. Rev.* **1962**, *128*, 1437. [CrossRef]
36. Jacob, C.R.; Reiher, M. Spin in density-functional theory. *Int. J. Quantum Chem.* **2012**, *112*, 3661–3684. [CrossRef]
37. Mahmoudi, S.; Dehkordi, M.M.; Asgarshamsi, M.H. Density functional theory studies of the antioxidants-a review. *J. Mol. Model.* **2021**, *27*, 271. [CrossRef]
38. Weinhold, F.; Landis, C.R.; Glendening, E.D. What is NBO analysis and how is it useful? *Int. Rev. Phys. Chem.* **2016**, *35*, 399–440. [CrossRef]
39. Alabugin, I.V.; Gilmore, K.M.; Peterson, P.W. Hyperconjugation. *Wiley Interdiscip. Rev.-Comput. Mol. Sci.* **2011**, *1*, 109–141. [CrossRef]
40. Spackman, M.A.; Jayatilaka, D. Hirshfeld surface analysis. *Crystengcomm* **2009**, *11*, 19–32. [CrossRef]
41. Spackman, M.A.; McKinnon, J.J. Fingerprinting intermolecular interactions in molecular crystals. *Crystengcomm* **2002**, *4*, 378–392. [CrossRef]
42. Hirshfeld, F.L. Bonded-atom fragments for describing molecular charge-densities. *Theor. Chim. Acta* **1977**, *44*, 129–138. [CrossRef]
43. Bader, R.F.W. Atoms in molecules. *Acc. Chem. Res.* **1985**, *18*, 9–15. [CrossRef]
44. Moreira, C.A.; Custodio, J.M.F.; Vaz, W.F.; D'Oliveira, G.D.C.; Perez, C.N.; Napolitano, H.B. A comprehensive study on crystal structure of a novel sulfonamide-dihydroquinolinone through experimental and theoretical approaches. *J. Mol. Model.* **2019**, *25*, 205. [CrossRef]
45. Custodio, J.M.F.; Gotardo, F.; Vaz, W.F.; D'Oliveira, G.D.C.; de Almeida, L.R.; Fonseca, R.D.; Cocca, L.H.Z.; Perez, C.N.; Oliver, A.G.; de Boni, L.; et al. Benzenesulfonyl incorporated chalcones: Synthesis, structural and optical properties. *J. Mol. Struct.* **2020**, *1208*, 127845. [CrossRef]
46. Perez, P.; Domingo, L.R.; Aurell, A.J.; Contreras, R. Quantitative characterization of the global electrophilicity pattern of some reagents involved in 1,3-dipolar cycloaddition reactions. *Tetrahedron* **2003**, *59*, 3117–3125. [CrossRef]
47. Domingo, L.R.; Aurell, M.J.; Perez, P.; Contreras, R. Quantitative characterization of the global electrophilicity power of common diene/dienophile pairs in Diels-Alder reactions. *Tetrahedron* **2002**, *58*, 4417–4423. [CrossRef]
48. Parr, R.G.; Yang, W.T. Density functional-approach to the frontier-electron theory of chemical-reactivity. *J. Am. Chem. Soc.* **1984**, *106*, 4049–4050. [CrossRef]
49. Gacche, R.N.; Dhole, N.A.; Kamble, S.G.; Bandgar, B.P. In-vitro evaluation of selected chalcones for antioxidant activity. *J. Enzym. Inhib. Med. Chem.* **2008**, *23*, 28–31. [CrossRef]
50. Anto, R.J.; Sukumaran, K.; Kuttan, G.; Rao, M.N.A.; Subbaraju, V.; Kuttan, R. Anticancer and antioxidant activity of synthetic chalcones and related-compounds. *Cancer Lett.* **1995**, *97*, 33–37. [CrossRef]
51. Wright, J.S.; Johnson, E.R.; DiLabio, G.A. Predicting the activity of phenolic antioxidants: Theoretical method, analysis of substituent effects, and application to major families of antioxidants. *J. Am. Chem. Soc.* **2001**, *123*, 1173–1183. [CrossRef]
52. Xue, Y.S.; Zheng, Y.G.; Zhang, L.; Wu, W.Y.; Yu, D.; Liu, Y. Theoretical study on the antioxidant properties of 2′-hydroxychalcones: H-atom vs. electron transfer mechanism. *J. Mol. Model.* **2013**, *19*, 3851–3862. [CrossRef] [PubMed]
53. Aguiar, A.S.N.; Borges, I.D.; Borges, L.L.; Dias, L.D.; Camargo, A.J.; Perjesi, P.; Napolitano, H.B. New Insights on Glutathione's Supramolecular Arrangement and Its In Silico Analysis as an Angiotensin-Converting Enzyme Inhibitor. *Molecules* **2022**, *27*, 7958. [CrossRef] [PubMed]
54. Bader, R.F.W.; Macdougall, P.J. Toward a theory of chemical-reactivity based on the charge-density. *J. Am. Chem. Soc.* **1985**, *107*, 6788–6795. [CrossRef]

55. Nakanishi, W.; Hayashi, S.; Itoh, N. Extended hypervalent 5c-6e interactions: Linear alignment of five C-Se—O—Se-C atoms in anthraquinone and 9-methoxyanthracene bearing arylselanyl groups at the 1,8-positions. *J. Org. Chem.* **2004**, *69*, 1676–1684. [CrossRef]
56. Nakanishi, W.; Hayashi, S.; Narahara, K. Polar Coordinate Representation of H-b(r(c)) versus ((h)over-bar(2)/8m)del(2)rho(b)(r(c)) at BCP in AIM Analysis: Classification and Evaluation of Weak to Strong Interactions. *J. Phys. Chem. A* **2009**, *113*, 10050–10057. [CrossRef]
57. Wheeler, O.H.; Gore, P.H.; Baez, R.; Santiago, M. Ultraviolet absorption of substituted phenyl + polycyclic aryl chalcones. *Can. J. Chem. -Rev. Can. Chim.* **1964**, *42*, 2580. [CrossRef]
58. Maragatham, G.; Selvarani, S.; Rajakumar, P.; Lakshmi, S. Structure determination and quantum chemical analysis of chalcone derivatives. *J. Mol. Struct.* **2019**, *1179*, 568–575. [CrossRef]
59. Lavakumar, S.; Vivekanand, P.A.; Prince, A.A.M. Simultaneous analysis of octylmethoxycinnamate and butylmethoxydibenzoylmethane in sunscreen products by a validated UV-spectrophotometric method. In Proceedings of National Conference on Chemistry and Materials (NCCM), Chennai, India, 22–23 March 2019; pp. 893–897.
60. Manaia, E.B.; Kaminski, R.C.K.; Correa, M.A.; Chiavacci, L.A. Inorganic UV filters. *Braz. J. Pharm. Sci.* **2013**, *49*, 201–209. [CrossRef]